Structural and dynamic basis of indirect apoptosis inhibition by Bcl-xL: a case study with Bid

Christina Elsner[1,†], Anton Hanke[2,3,†], Oscar Vadas[4], Francesco L. Gervasio[2,3,5,*], Enrica Bordignon[1,*]

[1]Department of Physical Chemistry, University of Geneva, 1211 Geneva, Switzerland

[2]Department of Pharmaceutical Sciences, University of Geneva, 1211 Geneva, Switzerland

[3]Swiss institute of Bioinformatics, University of Geneva, 1211 Geneva, Switzerland

[4]Department of Microbiology and Molecular Medicine, University of Geneva, 1211 Geneva, Switzerland

[5]Chemistry Department, University College London, WC1E 6BT London, United Kingdom

[*]Corresponding authors. Emails: `francesco.gervasio@unige.ch` and `enrica.bordignon@unige.ch`

[†]These authors contributed equally to this work.

Intrinsic apoptosis is a form of cell death which is activated, executed and inhibited by the Bcl-2 protein family. The structural basis of the inhibition mechanisms remains elusive. Here, we characterize the ensemble structure of the inhibitory Bcl-xL/tBid complex at the mitochondrial membrane by probing inter-residue distances and dynamic solvent accessibilities complemented by integrative modelling and molecular dynamics simulations. We show that Bcl-xL and tBid form a heterodimer anchored to the membrane by the C-terminal helix of Bcl-xL. The BH3 domain of tBid is wedged between the exposed hydrophobic groove of Bcl-xL and the membrane headgroups, while tBid's C-terminal helices remain dynamically engaged with the bilayer. This dynamic architecture sheds light on the mechanism of indirect inhibition of apoptosis.

Introduction

Apoptosis, a form of programmed cell death in multicellular eukaryotes, is a fundamental biological process; its dysregulation is implicated in the pathogenesis of numerous severe diseases [1–3]. The key step of the intrinsic pathway of apoptosis is the irreversible mitochondrial outer membrane permeabilization (MOMP), which is tightly controlled by the B-cell lymphoma 2 (Bcl-2)-protein family. Bcl-2 proteins are characterized by up to four Bcl-2 homology (BH) domains and, in most cases, a C-terminal transmembrane domain (TMD). Only the BH3 domain is common to all family members and essential for mediating their diverse interactions[4–7].

The Bcl-2 family is broadly divided into three subclasses. The first two are multi-BH-domain proteins: pro-apoptotic effectors (e.g., Bax, Bak, Bok) that oligomerize to permeabilize the mitochondrial outer membrane (MOM), and anti-apoptotic proteins (e.g., Bcl-2, Bcl-xL) that inhibit MOMP. The third subclass consists of the BH3-only proteins (e.g., Bim, Bid, Bad, PUMA), which act as either activators by directly triggering effectors or as sensitizers by neutralizing the anti-apoptotic proteins. These proteins dynamically exchange interaction partners, shuttling between the cytosol and the MOM in a process termed the "dance of death" [6]. This complex process involves substantial conformational changes and critically depends on interactions with the MOM (see for example [9–11]). To date, structural studies have primarily focused on the oligomeric state of effector proteins at the membrane. While the transformation of Bax and Bak from soluble monomers to membrane-bound oligomers is partially understood (see for example [12–17]), and recent cryo-EM structures have provided new clues about pore assembly based on tetrameric units[18], the topology of these oligomers within the membrane remains unclear. More critically, despite their relevance as therapeutic targets [19], the atomistic structures of inhibitory complexes between full-length anti-apoptotic proteins and their effector or activator partners remain unresolved. While analyses of truncated, water-soluble proteins have revealed a canonical BH3-in-groove binding mode [8, 11, 20–30], emerging evidence suggests that inhibitory interactions can involve more than one site [5, 31, 32]. This highlights the necessity of studying full-length proteins to fully elucidate the complex mechanism of inhibition. Here, we investigate the molecular basis for Bcl-xL's cytoprotective activity within a minimal, representative interaction network comprising the effector Bax, the activator cBid, and Bcl-xL itself (see Fig. 1). Using an integrative approach that combines modeling with extensive molecular dynamics (MD) simulations, constrained by available structural and topological data, we generated an atomistic model of the inhibitory Bcl-xL/tBid complex at the MOM which is validated by *in vitro* and *in organelle* data. The resulting structural ensemble reveals an inhibitory dimer with a distinct dynamic and flexible nature, anchored at the membrane via the Bcl-xL's

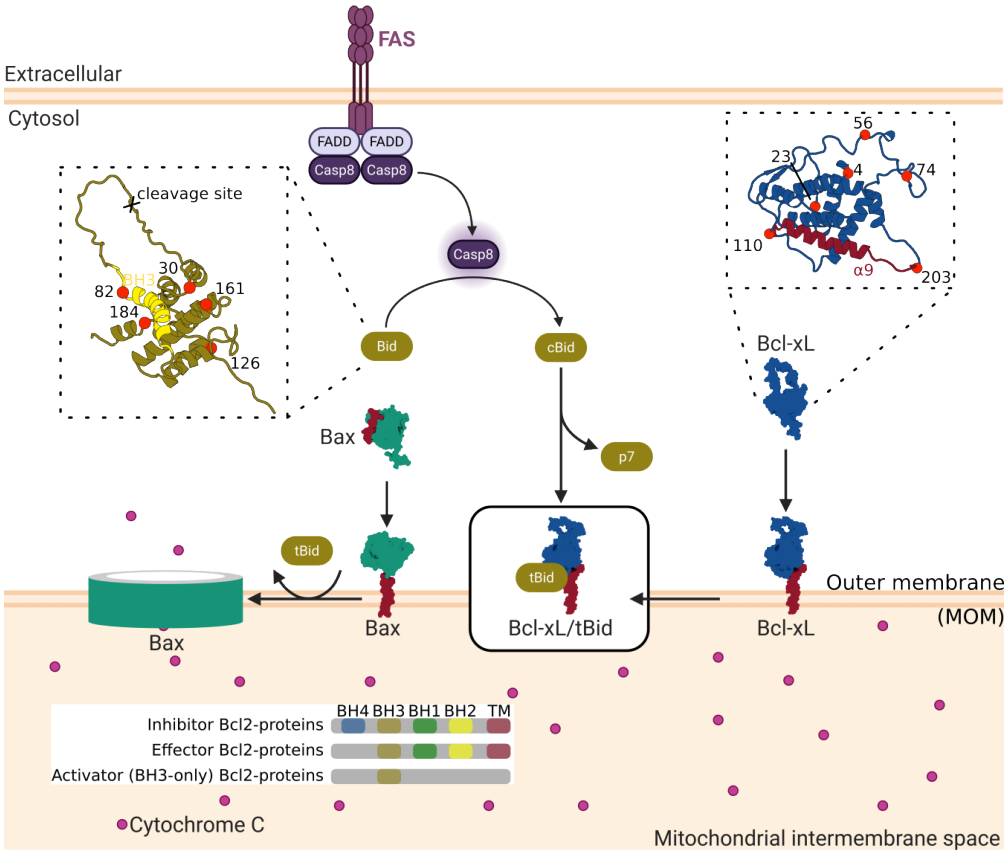

Figure 1: Scheme of the indirect inhibition of apoptosis in a minimal interaction network. External apoptotic stimuli activate Caspase 8, which cleaves Bid, producing cBid (consisting of the 7 kDa p7 fragment and the C-terminal 15 kDa tBid fragment). Monomeric Bax shuttles from the cytosol to the membrane via its C-terminal helix (dark red). At the membrane, the tBid fragment activates Bax, which forms oligomers permeabilizing the MOM (left). If tBid is sequestered by Bcl-xL at the membrane, membrane permeabilization is indirectly inhibited (right). The inset on the left shows the solution structure of mouse Bid (1DDB) with the helix containing the BH3 domain (yellow, BH3 domain: residues 87-100), the cleavage site in the loop and the spin labeling sites (red) indicated. The inset on the right shows the solution structure of full-length human Bcl-xL[8] with the C-terminal hydrophobic helix (dark red) and the spin labeling sites (red) indicated.

C-terminal helix and held together by tBid's BH3 domain sandwiched between the Bcl-xL's groove and the membrane headgroups.

Results

The Bcl-xL/tBid complex at the membrane is a dimer with both structured and flexible regions

We created a series of active spin-labeled single cysteine variants in cBid and Bcl-xL (see Fig. S1 and Fig. S2) for electron paramagnetic resonance (EPR) analysis. The chosen positions (n^{Bid} and $n^{\text{Bcl-xL}}$) are depicted on the available structural models of water-soluble mouse Bid and human Bcl-xL in Fig. 1 and of membrane-bound human tBid and Bcl-xL in Fig. 3. Bcl-xL and cBid have different propensities to interact with the membrane: Bcl-xL partitions between aqueous and membrane environments (see for example [8, 32, 33]), while cBid preferentially stays in solution [34]. Notably, if tBid is purified alone, it readily interacts with the membrane [35]. This characteristic partitioning is found also for the spin-labeled variants of cBid and Bcl-xL when incubated alone in presence of LUVs (Fig. 2B). In addition, when the two proteins are mixed with LUVs, the partitioning of Bcl-xL is not affected, while cBid increases its tendency to separate into two fragments, with tBid being enriched at the membrane (Fig. 2B), in agreement with previous data on the wild type proteins [11, 36]. The effect exerted by Bcl-xL on the partitioning of tBid at the membrane provides a first indication of the sequestration of the BH3-only activator protein in an inhibitory membrane-bound complex.

To structurally characterize this inhibitory complex, we measured a series of distance constraints between spin labels attached to cBid and Bcl-xL variants using Double Electron-Electron Resonance (DEER) spectroscopy (Fig. 2D,E). In the membrane-bound dimer, we found a defined distance between 82^{Bid}, a label located few residues before the BH3 domain, and $110^{\text{Bcl-xL}}$, a label located in the hydrophobic groove (Fig. 2D). The obtained distance is perfectly in line with the BH3-into-groove interaction expected from the available water soluble crystal structure (PDB 4QVE, predicted distances in Fig. S7). This proves that the BH3-into groove remains a key interaction between the two full-length proteins in the membrane-bound complex, confirming previous data obtained using full-length Bcl-xL and BH3-derived peptides (see for example [8, 37, 38]).

In addition, when each spin-labeled protein was mixed with its unlabeled partner, we could not detect specific Bcl-xL/Bcl-xL or cBid/cBid distances, proving that the inhibitory complex is a heterodimer and not a higher-order oligomer (Fig. 2D). Intriguingly, when probing the C-terminal region of cBid beyond residue 126, we could identify aspecific homo-interactions, indicating close proximity of the C-terminal regions of adjacent cBid proteins in the LUVs (see Fig. S6). All experimental Bcl-xL/cBid distances detected in the membrane-anchored heterodimer are presented in Fig. 2E. The first insight of the DEER analysis is that

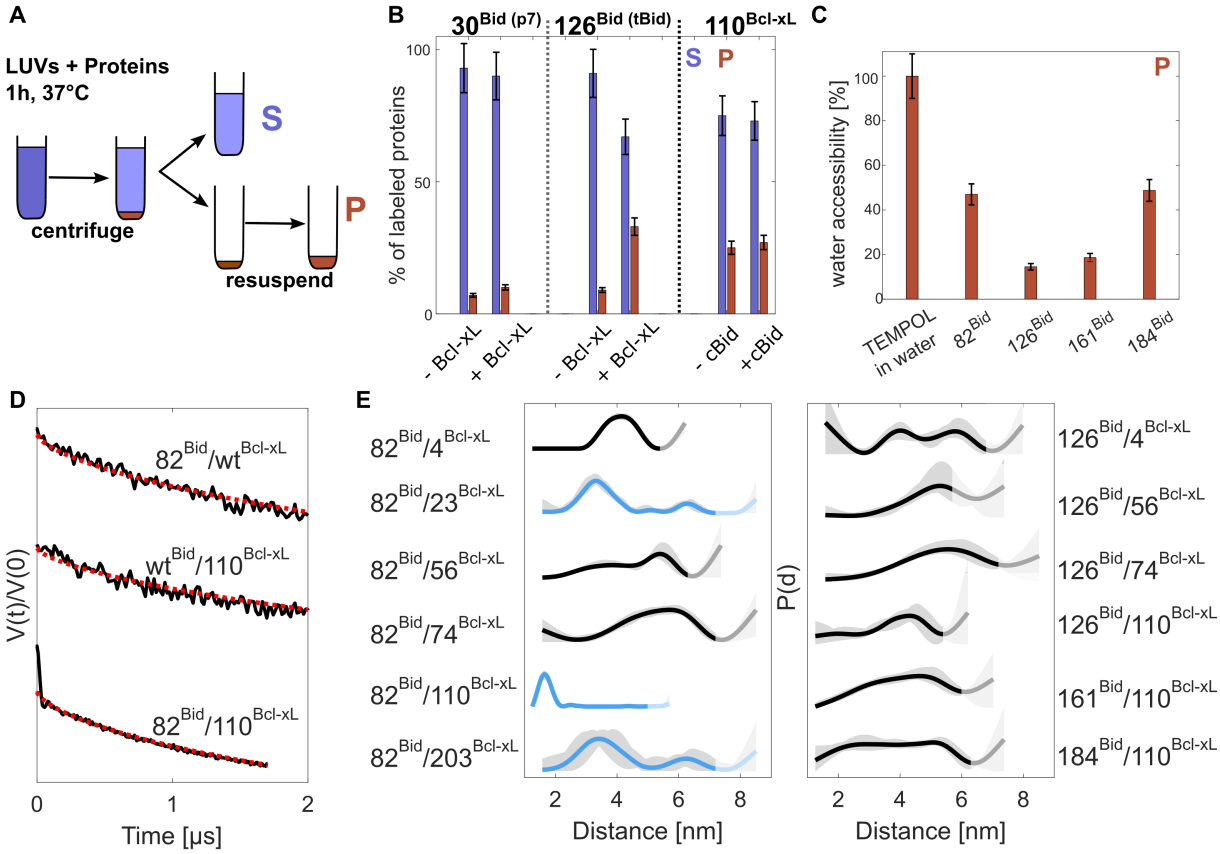

Figure 2: Experimental EPR data: cBid is sequestered by Bcl-xL at the membrane forming a heterodimer. (A) Scheme of the preparation of the aqueous (supernatant, S) and membrane (pellet, P) samples. **(B)** Fractions of p7 (30^{Bid}), tBid (126^{Bid}) and Bcl-xL ($110^{\text{Bcl-xL}}$) partitioning in the supernatant and pellet samples either alone (-) or in presence (+) of the corresponding unlabeled protein partner (EPR spectra in Fig. S3). **(C)** ESEEM analysis of the water accessibility of tBid in complex with Bcl-xL at the membrane (P). The 100% reference sample is the water soluble radical TEMPOL. Primary data in Fig. S4. **(D)** Primary DEER traces of the pellet samples of 82^{Bid} incubated with unlabeled wild type Bcl-xL; unlabeled wild type cBid incubated with $110^{\text{Bcl-xL}}$; labeled 82^{Bid} and $110^{\text{Bcl-xL}}$ incubated together. The two upper traces (only one protein is labeled) are indistinguishable from a 2-dimensional background (red dotted), indicating the absence of specific homo-dimeric interactions. The bottom trace (one spin label in each protein) shows distinct dipolar oscillations due to the formation of a heterodimer. **(E)** Distance distributions (black, with shaded grey area representing the uncertainties) of different combinations of labeled cBid/Bcl-xL variants. Three distance constraints used for the initial MD model are in light blue. The shading of the distance distribution at long distances indicates the cutoff of the distance reliability. Primary data and additional DEER traces can be found in Fig. S5, S6, S7 and S8.

the BH3 domain of cBid (82^{Bid}) has defined distances to residues in the globular region of Bcl-xL with full width at half maximum $< 1.5\,nm$ (compatible with the rotational freedom of the spin labels attached), indicating a tight binding of BH3 to Bcl-xL in the complex. Notably, broader distance distributions ($> 2\,nm$) between the BH3 domain of cBid and two

residues in the long $\alpha 1/2$ loop of Bcl-xL ($56^{\text{Bcl-xL}}$, $74^{\text{Bcl-xL}}$) confirm that the loop of Bcl-xL remains flexible in the complex. The second insight is that the region of cBid following the BH3 domain is highly disordered, with distance distributions $> 3\,nm$ (Fig. 2E). In addition, based on the low accessibility towards deuterated water in the sample (detected via Electron Spin Echo Envelope Modulation, ESEEM), the C-terminal region of cBid is also found to be partially shielded from bulk water, suggesting its proximity to the membrane (Fig. 2 C).

Building the initial model of the Bcl-xL/tBid heterodimer

An initial model of the membrane-anchored human Bcl-xL/tBid complex was created with Modeller [39] following an integrative approach, combining existing partial experimental structures, homology modelling, and experimental observables [40]. The structures of the membrane-associated human tBid (PDB 2M5I [35], 64% sequence identity with the mouse Bid used for the DEER distance constraints, Fig. S9), a truncated aqueous complex of human Bcl-xL and a BH3 peptide from human Bid (PDB 4QVE [21]), and a model of the full-length membrane-embedded human Bcl-xL [8] were used as templates for the complex between tBid and Bcl-xL (see Fig. 3A). The template structures were positioned by aligning common structural regions. The EPR data on the water accessibility of cBid's $\alpha 4-8$ helices (see Fig. 2) were used to re-orient the helices of tBid towards the membrane (as described in the Methods) (see Fig. S10).

Model generation was also guided by three experimental label-label distances between the BH3 domain of cBid and $\alpha 1$, $\alpha 3$, $\alpha 8$ of Bcl-xL (see Fig. 2D light blue lines). The resulting ten models showed a satisfactory initial agreement between the predicted and experimental label-label distances (see Fig. 3B). The model showing the best agreement to the EPR distances (Fig. 3C, see Methods) was used to run unrestrained MD simulations ($7 \times 1\,\mu s$).

A dynamic Bcl-xL/tBid inhibitory complex at the membrane

The unrestrained MD-derived ensemble is characterised by both structured and highly flexible regions in the complex (Fig. 4A,B,C), in line with the experimental EPR data (Fig. 2E). Four independently moving domains could be identified within the complex (see Fig. 4D).

The BH3 domain of tBid remains tightly bound to Bcl-xL's globular domain (see Fig. 4D and table S1), forming the largest independently moving domain. In contrast to the published aqueous structure [21], the BH3 is sandwiched between the canonical binding groove and the membrane (see Fig. 4E) with the groove of Bcl-xL moving away from the

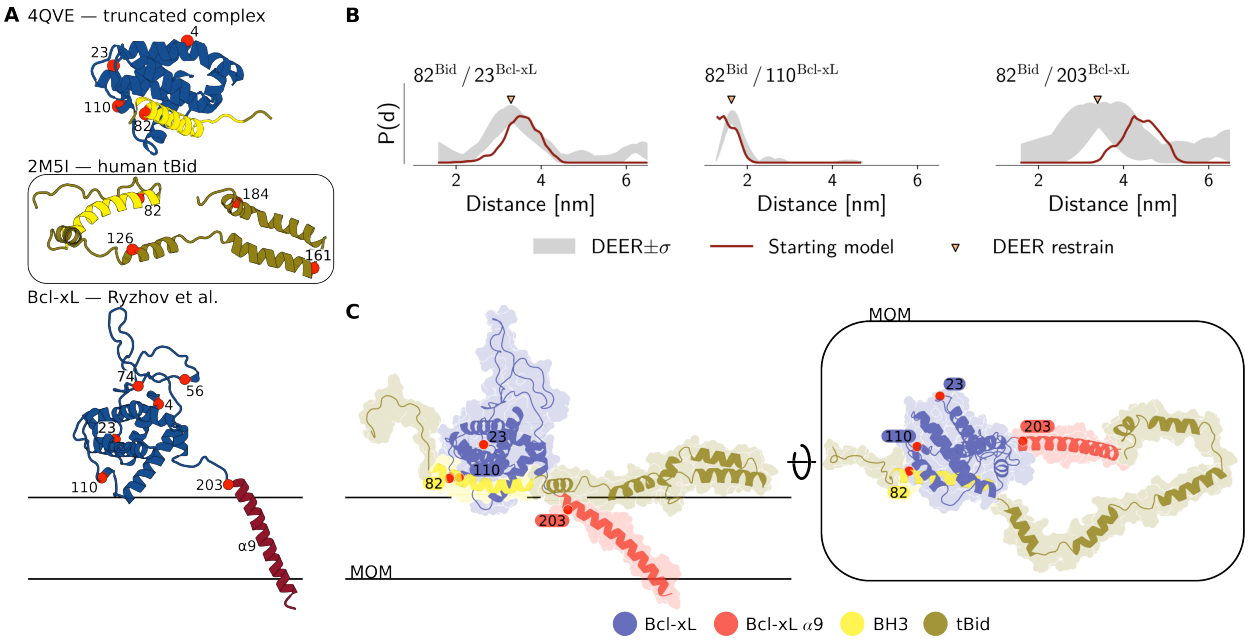

Figure 3: Initial model of the Bcl-xL/tBid complex at the membrane. (A) Reference structures used as basis for the homology modelling [8, 21, 35] **(B)** Three distance constraints (orange triangles) from Fig. 2E used to refine the starting model together with the ESEEM accessibility data from Fig. 2C . In red, the distance distributions calculated with DEER-PREdict [41] on the generated starting models. **(C)** Cartoon and surface representation of the starting model used for subsequent unbiased MD simulations. Label positions are indicated as red circles, the membrane (MOM) is indicated with black lines. The model was generated with Modeller [39].

membrane headgroup region upon tBid binding. The second largest domain consists of the tBid C-terminal helices freely diffusing on the membrane (see Fig. 4D and Fig. S12C, E), adopting both compact C-shaped conformations and extended conformations (see Fig. 4B). The complex is membrane-anchored via the $\alpha 9$ (see Fig. 4D) of Bcl-xL, which moves independently from the largest domains (see Fig. S13). This TMD retains a tilted orientation in relation to the membrane normal (see Fig. 4F), as shown in previous studies [8]. The globular domain of Bcl-xL contacts the membrane predominantly via the $\alpha 2$ helix, the C-terminal tip of the $\alpha 1$ helix, the $\alpha 8$ helix, and transiently also via the $\alpha 4/5$ loop (see Fig. S12C). The remaining smaller domain is the flexible $\alpha 1/2$ loop of Bcl-xL (see Fig. 4D,C,G), whose flexibility increases upon binding to tBid (see Fig. S13). Notably binding of tBid also shifts dynamics in the binding site of Bcl-xL, rigidifying the $\alpha 3$ helix and destabilizing the $\alpha 4$ helix (see Fig. S13). To summarize, Bcl-xL sequesters tBid at the membrane by sandwiching its BH3 domain between the canonical hydrophobic groove and the membrane's headgroups. The resulting complex is a highly flexible heterodimer, tethered via the Bcl-xL's $\alpha 9$ helix to the membrane, with the C-terminal region of tBid freely diffusing on the membrane.

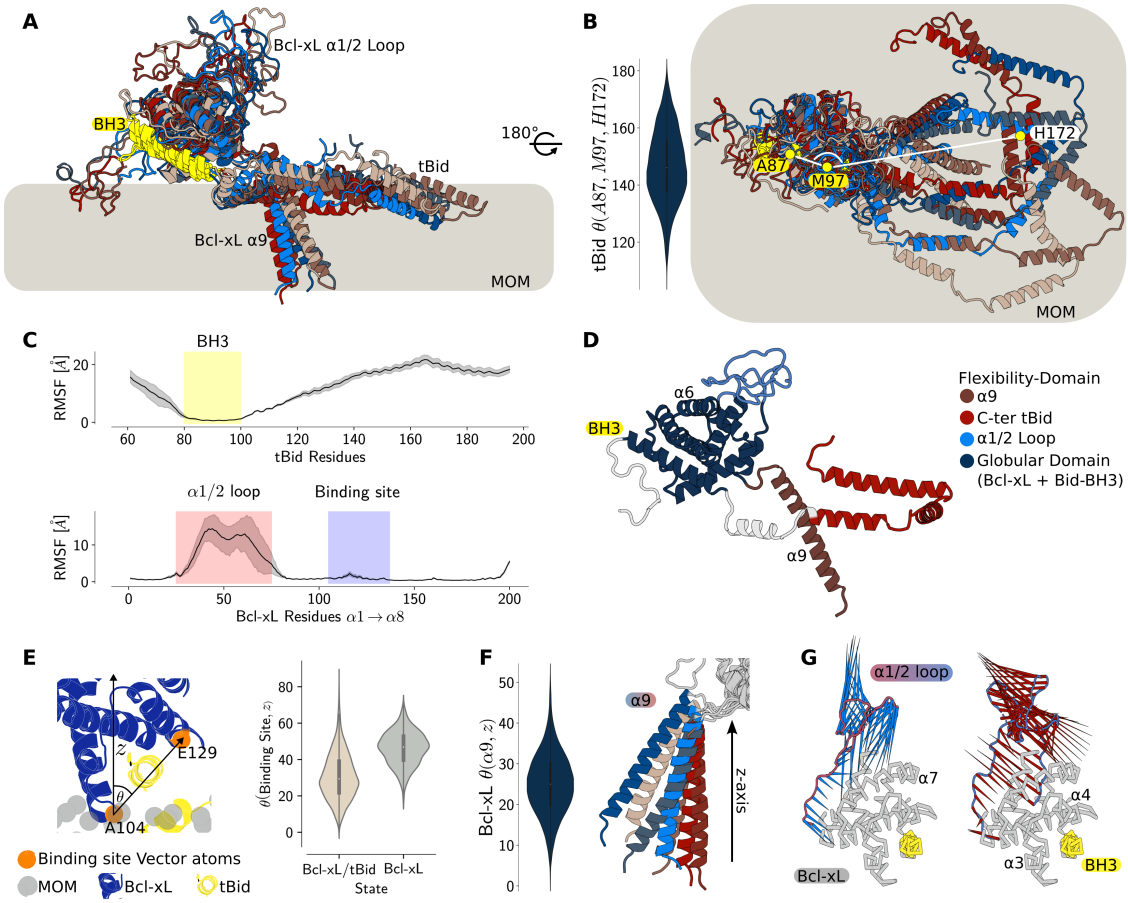

Figure 4: Structured and dynamic regions coexist in the Bcl-xL/tBid heterodimer. **(A)** Cluster representatives of the Bcl-xL/tBid complex structural ensemble embedded on a lipid membrane (cartoon, side view). The tightly bound BH3 domain is shown in yellow. **(B)** tBid's helices $\alpha 4 - 8$ diffuse freely on the membrane (cartoon, top view), as shown by their angular spread with respect to the BH3 domain (angle-defining atoms as yellow spheres). **(C)** Root mean square fluctuations (RMSF) of tBid and Bcl-xL. Structures were aligned on the $\alpha 5$ and $\alpha 6$ helical Cα-atoms of Bcl-xL. Specific regions of the sequences are highlighted. **(D)** Four independently moving domains were identified based on standard deviation of residue-residue distances. **(E)** The hydrophobic groove of Bcl-xL is tilted away from the membrane when tBid is bound. The binding site is shown as cartoon (Bcl-xL: blue; tBid: yellow). The plot shows the comparison of the angular spread of the binding site of Bcl-xL alone or in complex with tBid (vector connecting A104 and E129, orange spheres) with respect to the membrane normal (z). **(F)** Angular spread of the $\alpha 9$ of Bcl-xL with respect to the membrane normal (z). Cluster representatives are shown aligned on the globular domain of Bcl-xL. **(G)** The $\alpha 1/2$ loop of Bcl-xL remains highly flexible in the heterodimer, as shown by porcupine plots of the first two principle components of the loop atom displacement (Bcl-xL: grey; tBid's BH3 helix: yellow). Additional information can be found in Fig. S11 to Fig. S13.

In vitro and *in organelle* experiments validate the Bcl-xL/tBid complex

The atomistic Bcl-xL/tBid model was validated through independent experiments *in vitro* and *in organelle*. First, hydrogen deuterium exchange mass spectrometry (HDX-MS) was

used to probe the solvent accessibility of the complex in LUVs, highlighting fold dynamics, membrane-protein and protein-protein interactions. Deuterium exchange patterns within Bcl-xL from the water soluble to the membrane-embedded state confirm the membrane-embedding of the $\alpha 9$ helix in Bcl-xL alone and in presence of cBid, with decreased relative deuteration in the latter case (see Fig. S14). Simulations on the ensemble Bcl-xL/tBid dimeric structure show excellent correlation with the experimental deuteration patterns of Bcl-xL in the membrane fraction in presence of cBid ($0.82 \leq R^2 \leq 0.91$) (Fig. 5B), which validated structure, dynamics and topology of the anti-apoptotic protein in the complex. The experimental HDX pattern of cBid indicates an increase in the protein's deuteration and flexibility going from the water-soluble form to the complex with Bcl-xL at the membrane (see Fig. S16), corroborating the high flexibility observed in the C-terminal region of tBid in the dimeric ensemble (see Fig. 4C). The simulated HDX data on the heterodimeric ensemble between Bcl-xL and human tBid show a reasonable correlation ($0.18 \leq R^2 \leq 0.45$) with the experimental patterns (Fig. 5C). The minor discrepancies observed might be due to the small variations in the peptide sequences in mouse/human tBid and the presence of residual water soluble cBid in the sample (see Fig. 4C and Fig. S16).

In a second step the dynamic structure of the inhibitory complex was further validated by comparison of the label-label DEER distance distributions predicted on the whole MD trajectories with the experimental data (see Fig. 5 A). The agreement between simulations and *in vitro* distance constraints is good and lies within the expected root mean square deviations of the rotamer library approach used[43]. The DEER validation therefore supports the binding mode between Bcl-xL's structured region and tBid's BH3 domain (82^{Bid}) (Fig. 5D). A discrepancy was identified in the shape of the $82^{\text{Bid}} - 74^{\text{Bcl-xL}}$ distance distribution, which was narrower in the ensemble than in the experiments (Fig. 5D). A detailed analysis of the loop dynamics showed that the spin label at position 74 within the $\alpha 1/2$ loop of Bcl-xL might have affected the dynamics of the electrostatic cluster of residues (see Fig. S19). The under-represented longer distances in the ensemble arise from snapshots where such electrostatic lock is weaker or disrupted (see Fig. S19).

The broad calculated distance distributions between Bcl-xL and the flexible C-terminal helices (126^{Bid}) also agree with the experimental data (Fig. 5E). We noted that the predicted $126^{\text{Bid}} - 110^{\text{Bcl-xL}}$ distances (Fig. 5D) show contributions only above 5 nm, missing the shorter distances experimentally detected. This discrepancy is intriguing, because all distance constraints involving $110^{\text{Bcl-xL}}$ are well described by the ensemble, therefore it must arise from the localization of residue 126. This suggests an even larger heterogeneity in the relative orientation of the C-terminal region of tBid around Bcl-xL than that captured in the ensemble. Lastly, to corroborate the physiological relevance of this dynamic inhibitory

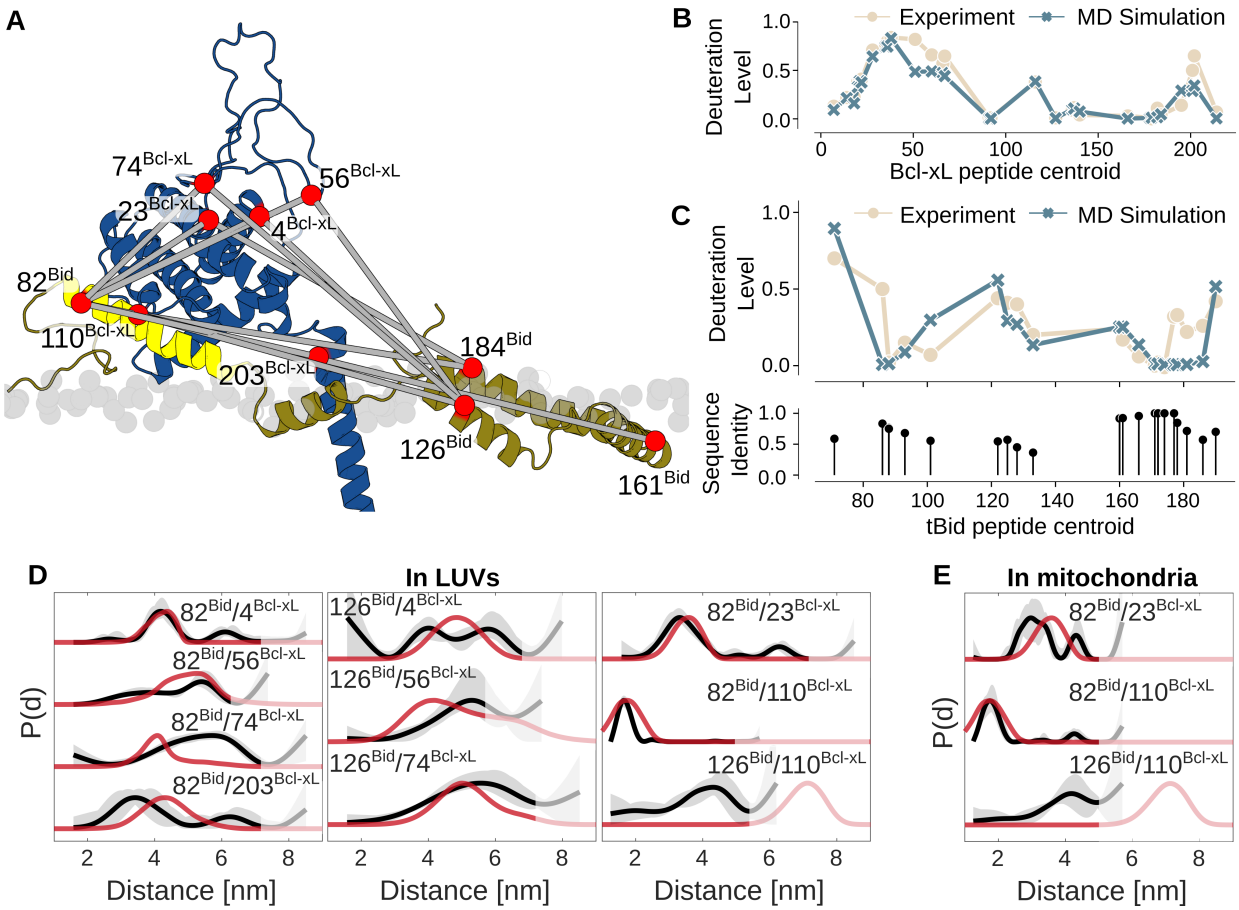

Figure 5: Experimental validation of the structural ensemble. (A) Representative cartoon structure of the tBid/Bcl-xL complex (blue: Bcl-xL, yellow: BH3 domain of tBid, dark yellow: tBid, light grey: lipid phosphates) with indicated label positions (red spheres) and experimental distances (grey lines). **(B)** Experimental (beige, pellet fraction after incubation of cBid with Bcl-xL and LUVs) versus simulated (blue, Bcl-xL/tBid complex) deuterium uptake of Bcl-xL peptides (additional data in Figs. S14, S15). **(C)** Experimental (beige, pellet fraction after incubation of cBid with Bcl-xL and LUVs) versus simulated (blue, Bcl-xL/tBid complex) deuterium uptake of tBid peptides (additional data in Figs. S15, S16). The sequence identity between human (MD simulation) and mouse (experiment) tBid for the detected peptides is shown. **(D)** Experimental DEER distance distributions (black with grey area representing the uncertainty and the shaded region indicating the cutoff for reliable distances according to [42]) compared to those calculated on the MD simulation trajectories using DEER-PREdict (red). Additional distance distributions, technical and biological repeats, primary data, and analysis in Figs. S7, S8 and S19. **(E)** *In organelle* distance distributions (color code as in panel D) compared to the corresponding calculated distance distributions. Additional information can be found in Figs. S17, S18 and S21.

complex, we investigated three key distances in isolated mitochondria from mouse liver. The inhibitory Bcl-xL/tBid complex formed in mitochondria was found to retain the same distance constraints found *in vitro* between the BH3 domain and Bcl-xL's globular domain, and the broad distance distributions between tBid's C-terminal helices and Bcl-xL (see Fig. 5E). The data in mitochondria confirm that tBid binds Bcl-xL's hydrophobic groove via its

BH3 domain and that the following helices have a high degree of flexibility.

Discussion

Resolving the interaction mode of MOM-associated Bcl-2 inhibitory complexes is crucial for understanding the regulation of apoptosis and for developing potent apoptotic modulators. Here, using an integrative modeling approach that combines experimental data with molecular simulations, we describe the structure, interaction interfaces, and dynamics of the inhibitory complex between Bcl-xL and tBid at the mitochondrial outer membrane.

Bcl-xL has been reported to shuttle between the cytosol and the membrane[33, 44]. Its membrane-anchored form is responsible for sequestering tBid in the indirect MOMP inhibition mode. By competing with p7 [34], Bcl-xL shifts tBid's equilibrium towards the membrane-bound form and finally sequesters it. Our analysis reveals a structural dichotomy in the membrane-bound Bcl-xL/tBid complex. While tBid's BH3 domain is firmly locked between Bcl-xL's hydrophobic groove and the membrane bilayer, impeding any interaction with effector proteins, its C-terminal region remains flexible and diffuses freely across the membrane surface. This mobile C-terminus, together with the TMD of Bcl-xL, forms the complex's extensive membrane-interaction surface (Fig. 4D and Fig. S12E). These flexible regions may even permit loose interactions between adjacent heterodimers. Whether such crowding contributes to the sequestration mechanism or regulates interactions with other BH3-only proteins remains an open question. This inhibitory mechanism highlights the crucial role of the MOM in shaping the binding interface, a feature necessarily absent in previous studies using truncated, water-soluble proteins. Although we did not simulate the initial binding event, our model reveals its structural consequence: the globular domain of membrane-anchored Bcl-xL repositions itself away from the membrane upon tBid binding. This movement exposes the hydrophobic groove, allowing the BH3 domain to be sandwiched against the membrane's headgroup region. This coordinated motion effectively locks the BH3 helix from three sides, in stark contrast to the more accessible binding site of truncated Bcl-xL variants in solution [21]. Notably, this observation aligns with the proposed "cryptic" nature of Bcl-xL's binding pocket, which is thought to require unfolding for ligand access [45–47]. Indeed, the α3 helix, which was unfolded in our starting model [8], remains so throughout our simulations, suggesting the membrane environment primes the binding groove for engagement with tBid. We find that Bcl-xL sequesters pro-apoptotic tBid exclusively at the membrane, as any interaction in the cytosol is sterically prohibited. This prevention occurs because the BH3 domain of cBid is occluded by its p7 fragment, while the corresponding binding groove on Bcl-xL is blocked by its own α9 helix. The membrane

is therefore an essential component of the inhibitory complex, which recruits the protein partners, shapes the BH3 binding site and allows the flexibility of the C-terminal helices of tBid. Indeed, AlphaFold2 [48] fails to correctly predict the topology and assembly of the inhibitory complex due to the lack of the membrane environment (see Fig. S20).

The mechanism of tBid inhibition fundamentally differs from how Bcl-xL inhibits Bim, a BH3-only protein that, unlike Bid, contains a C-terminal transmembrane domain (TMD) [49]. Bcl-xL was found to neutralize Bim via a "double-bolt" lock mechanism, engaging both the canonical BH3-groove interface and a direct TMD-TMD interaction. This robust, dual-mode sequestration might contribute to cellular resistance against BH3-mimetic drugs that target only the binding groove. In addition, Bcl-xL was found to inhibit apoptosis as a higher-order complex that binds multiple BH3 proteins [32]. The existence of distinct inhibitory strategies will require development of therapeutic approaches tailored to specific protein-protein and protein-membrane interfaces [44, 49–52]. Elucidating the structural basis for the diverse inhibitory mechanisms within the Bcl-2 family is therefore paramount for designing next-generation therapies.

Bibliography

(1) Yuan, J.; Ofengeim, D. *Nature Reviews Molecular Cell Biology* **2024**, *25*, Publisher: Nature Publishing Group, 379–395.

(2) Galluzzi, L. et al. *Cell Death & Differentiation* **2018**, *25*, Publisher: Nature Publishing Group, 486–541.

(3) Vitale, I. et al. *Cell Death & Differentiation* **2023**, *30*, 1097–1154.

(4) Tait, S. W. G.; Green, D. R. *Nature Reviews Molecular Cell Biology* **2010**, *11*, 621–632.

(5) Nguyen, D.; Osterlund, E.; Kale, J.; Andrews, D. W. *Biochemical Journal* **2024**, *481*, 903–922.

(6) Kale, J.; Osterlund, E. J.; Andrews, D. W. *Cell Death & Differentiation* **2018**, *25*, 65–80.

(7) Czabotar, P. E.; Garcia-Saez, A. J. *Nature Reviews Molecular Cell Biology* **2023**, 1–17.

(8) Ryzhov, P.; Tian, Y.; Yao, Y.; Bobkov, A. A.; Im, W.; Marassi, F. M. *Biophysical Journal* **2020**, *119*, 1324–1334.

(9) García-Sáez, A. J.; Ries, J.; Orzáez, M.; Pérez-Payà, E.; Schwille, P. *Nature Structural & Molecular Biology* **2009**, *16*, 1178–1185.

(10) Rose, M.; Kurylowicz, M.; Mahmood, M.; Winkel, S.; Moran-Mirabal, J. M.; Fradin, C. *International Journal of Molecular Sciences* **2021**, *22*, 8240.

(11) Murad, F.; J. Garcia-Saez, A. *Faraday Discussions* **2021**, *232*, 86–102.

(12) Oh, K. J.; Singh, P.; Lee, K.; Foss, K.; Lee, S.; Park, M.; Lee, S.; Aluvila, S.; Park, M.; Singh, P.; Kim, R.-S.; Symersky, J.; Walters, D. E. *Journal of Biological Chemistry* **2010**, *285*, 28924–28937.

(13) Bleicken, S.; Jeschke, G.; Stegmueller, C.; Salvador-Gallego, R.; García-Sáez, A. J.; Bordignon, E. *Molecular Cell* **2014**, *56*, 496–505.

(14) Cowan, A. D. et al. *Nature Structural & Molecular Biology* **2020**, *27*, 1024–1031.

(15) Lv, F. et al. *The EMBO Journal* **2021**, *40*, e106438.

(16) Birkinshaw, R. W.; Iyer, S.; Lio, D.; Luo, C. S.; Brouwer, J. M.; Miller, M. S.; Robin, A. Y.; Uren, R. T.; Dewson, G.; Kluck, R. M.; Colman, P. M.; Czabotar, P. E. *Molecular Cell* **2021**, *81*, 2123–2134.e5.

(17) Clifton, L. A.; Wacklin-Knecht, H. P.; Ådén, J.; Mushtaq, A. U.; Sparrman, T.; Gröbner, G. *Science Advances* **2023**, *9*, eadg7940.

(18) Zhang, Y.; Tian, L.; Huang, G.; Ge, X.; Kong, F.; Wang, P.; Xu, Y.; Shi, Y. *Science* **2025**, *388*, eadv4314.

(19) Tanaka, Y. et al. *Journal of Medicinal Chemistry* **2013**, *56*, 9635–9645.

(20) Campbell, S. T.; Carlson, K. J.; Buchholz, C. J.; Helmers, M. R.; Ghosh, I. *Biochemistry* **2015**, *54*, 2632–2643.

(21) Rajan, S.; Choi, M.; Baek, K.; Yoon, H. S. *Proteins: Structure, Function, and Bioinformatics* **2015**, *83*, 1262–1272.

(22) Czabotar, P. E.; Lee, E. F.; Thompson, G. V.; Wardak, A. Z.; Fairlie, W. D.; Colman, P. M. *Journal of Biological Chemistry* **2011**, *286*, 7123–7131.

(23) Lee, E. F.; Smith, B. J.; Horne, W. S.; Mayer, K. N.; Evangelista, M.; Colman, P. M.; Gellman, S. H.; Fairlie, W. D. *ChemBioChem* **2011**, *12*, 2025–2032.

(24) Rajan, S.; Choi, M.; Nguyen, Q. T.; Ye, H.; Liu, W.; Toh, H. T.; Kang, C.; Kamariah, N.; Li, C.; Huang, H.; White, C.; Baek, K.; Grüber, G.; Yoon, H. S. *Scientific Reports* **2015**, *5*, 10609.

(25) Ambrosi, E.; Capaldi, S.; Bovi, M.; Saccomani, G.; Perduca, M.; Monaco, H. L. *Biochemical Journal* **2011**, *438*, 291–301.

(26) Follis, A. V.; Chipuk, J. E.; Fisher, J. C.; Yun, M.-K.; Grace, C. R.; Nourse, A.; Baran, K.; Ou, L.; Min, L.; White, S. W.; Green, D. R.; Kriwacki, R. W. *Nature Chemical Biology* **2013**, *9*, 163–168.

(27) Petros, A. M.; Nettesheim, D. G.; Wang, Y.; Olejniczak, E. T.; Meadows, R. P.; Mack, J.; Swift, K.; Matayoshi, E. D.; Zhang, H.; Fesik, S. W.; Thompson, C. B. *Protein Science* **2000**, *9*, 2528–2534.

(28) Sattler, M.; Liang, H.; Nettesheim, D.; Meadows, R. P.; Harlan, J. E.; Eberstadt, M.; Yoon, H. S.; Shuker, S. B.; Chang, B. S.; Minn, A. J.; Thompson, C. B.; Fesik, S. W. *Science* **1997**, *275*, 983–986.

(29) Lee, E. F.; Dewson, G.; Evangelista, M.; Pettikiriarachchi, A.; Gold, G. J.; Zhu, H.; Colman, P. M.; Fairlie, W. D. *Journal of Biological Chemistry* **2014**, *289*, 36001–36017.

(30) O'Neill, J. W.; Manion, M. K.; Maguire, B.; Hockenbery, D. M. *Journal of Molecular Biology* **2006**, *356*, 367–381.

(31) Ding, J.; Mooers, B. H.; Zhang, Z.; Kale, J.; Falcone, D.; McNichol, J.; Huang, B.; Zhang, X. C.; Xing, C.; Andrews, D. W.; Lin, J. *Journal of Biological Chemistry* **2014**, *289*, 11873–11896.

(32) Bogner, C.; Kale, J.; Pogmore, J.; Chi, X.; Shamas-Din, A.; Fradin, C.; Leber, B.; Andrews, D. W. *Molecular Cell* **2020**, *77*, 901–912.e9.

(33) Hsu, Y.-T.; Wolter, K. G.; Youle, R. J. *Proceedings of the National Academy of Sciences* **1997**, *94*, 3668–3672.

(34) Bleicken, S.; García-Sáez, A. J.; Conte, E.; Bordignon, E. *PLoS ONE* **2012**, *7*, ed. by Bratton, S. B., e35910.

(35) Wang, Y.; Tjandra, N. *Journal of Biological Chemistry* **2013**, *288*, 35840–35851.

(36) Elsner, C.; Epasto, L. M.; Cieren, A.; Gendreizig, D.; Kucher, S.; Roderer, D.; Bordignon, E. Characterization of the direct and indirect inhibition of apoptosis by full-length recombinant Bcl-xL monomers, en, 2025.

(37) Raltchev, K.; Pipercevic, J.; Hagn, F. *Chemistry – A European Journal* **2018**, *24*, _eprint: https://chemistry-europe.onlinelibrary.wiley.com/doi/pdf/10.1002/chem.201800812, 5493–5499.

(38) Pogmore, J. P.; Pemberton, J. M.; Chi, X.; Andrews, D. W. *Methods in Molecular Biology (Clifton, N.J.)* **2016**, *1419*, 197–212.

(39) Eswar, N.; Eramian, D.; Webb, B.; Shen, M.-Y.; Sali, A. *Structural Proteomics* **2008**, 145–159.

(40) Webb, B.; Sali, A. *Current Protocols in Bioinformatics* **2016**, *54*, 5.6.1–5.6.37.

(41) Tesei, G.; Martins, J. M.; Kunze, M. B. A.; Wang, Y.; Crehuet, R.; Lindorff-Larsen, K. *PLOS Computational Biology* **2021**, *17*, e1008551.

(42) Jeschke, G. *Annual Review of Physical Chemistry* **2012**, *63*, 419–446.

(43) Jeschke, G. *Progress in Nuclear Magnetic Resonance Spectroscopy* **2013**, *72*, 42–60.

(44) Aranovich, A.; Liu, Q.; Collins, T.; Geng, F.; Dixit, S.; Leber, B.; Andrews, D. W. *Molecular Cell* **2012**, *45*, 754–763.

(45) Liu, X.; Beugelsdijk, A.; Chen, J. *Biophysical Journal* **2015**, *109*, 1049–1057.

(46) Bekker, G.-J.; Araki, M.; Oshima, K.; Okuno, Y.; Kamiya, N. *Communications Biology* **2023**, *6*, 1–11.

(47) Muchmore, S. W.; Sattler, M.; Liang, H.; Meadows, R. P.; Harlan, J. E.; Yoon, H. S.; Nettesheim, D.; Chang, B. S.; Thompson, C. B.; Wong, S.-L.; Ng, S.-C.; Fesik, S. W. *Nature* **1996**, *381*, 335–341.

(48) Mirdita, M.; Schütze, K.; Moriwaki, Y.; Heo, L.; Ovchinnikov, S.; Steinegger, M. *Nature Methods* **2022**, *19*, 679–682.

(49) Liu, Q.; Osterlund, E. J.; Chi, X.; Pogmore, J.; Leber, B.; Andrews, D. W. *eLife* **2019**, *8*, Publisher: eLife Sciences Publications, Ltd, DOI: `10.7554/elife.37689`.

(50) Mérino, D. et al. *Blood* **2012**, *119*, 5807–5816.

(51) Liu, Q.; Leber, B.; Andrews, D. W. *Cell Cycle* **2012**, *11*, 3536–3542.

(52) Pécot, J.; Maillet, L.; Le Pen, J.; Vuillier, C.; Trécesson, S. D. C.; Fétiveau, A.; Sarosiek, K. A.; Bock, F. J.; Braun, F.; Letai, A.; Tait, S. W.; Gautier, F.; Juin, P. P. *Cell Reports* **2016**, *17*, 3347–3358.

(53) Desagher, S.; Osen-Sand, A.; Nichols, A.; Eskes, R.; Montessuit, S.; Lauper, S.; Maundrell, K.; Antonsson, B.; Martinou, J.-C. *The Journal of Cell Biology* **1999**, *144*, 891–901.

(54) Suzuki, M.; Youle, R. J.; Tjandra, N. *Cell* **2000**, *103*, 645–654.

(55) Bleicken, S.; Wagner, C.; García-Sáez, A. J. *Biophysical Journal* **2013**, *104*, 421–431.

(56) Teucher, M.; Bordignon, E. *Journal of Magnetic Resonance* **2018**, *296*, 103–111.

(57) Jeschke, G.; Chechik, V.; Ionita, P.; Godt, A.; Zimmermann, H.; Banham, J.; Timmel, C. R.; Hilger, D.; Jung, H. *Applied Magnetic Resonance* **2006**, *30*, 473–498.

(58) Wang, H.; Lo, W.-T.; Vujičić Žagar, A.; Gulluni, F.; Lehmann, M.; Scapozza, L.; Haucke, V.; Vadas, O. *Molecular Cell* **2018**, *71*, 343–351.e4.

(59) Frezza, C.; Cipolat, S.; Scorrano, L. *Nature Protocols* **2007**, *2*, 287–295.

(60) Schrödinger, LLC The PyMOL molecular graphics system, version 1.8, 2015.

(61) Jeschke, G. *Protein Science* **2024**, *33*, _eprint: https://onlinelibrary.wiley.com/doi/pdf/10.1002/p
e4906.

(62) Dolinsky, T. J.; Czodrowski, P.; Li, H.; Nielsen, J. E.; Jensen, J. H.; Klebe, G.; Baker, N. A. *Nucleic Acids Research* **2007**, *35*, W522–W525.

(63) Olsson, M. H. M.; Søndergaard, C. R.; Rostkowski, M.; Jensen, J. H. *Journal of Chemical Theory and Computation* **2011**, *7*, 525–537.

(64) Lee, J.; Cheng, X.; Swails, J. M.; Yeom, M. S.; Eastman, P. K.; Lemkul, J. A.; Wei, S.; Buckner, J.; Jeong, J. C.; Qi, Y.; al. et, e. *Journal of Chemical Theory and Computation* **2015**, *12*, 405–413.

(65) Jing Huang; Sarah Rauscher; Grzegorz Nawrocki; Ting Ran; Michael Feig; Bert L de Groot; Helmut Grubmüller; Alexander D MacKerell *Nature Methods* **2016**, *14*, Publisher: Springer Science and Business Media LLC, 71–73.

(66) Marchi, M.; Ballone, P. *The Journal of Chemical Physics* **1999**, *110*, 3697–3702.

(67) Van Der Spoel, D.; Lindahl, E.; Hess, B.; Groenhof, G.; Mark, A. E.; Berendsen, H. J. C. *Journal of Computational Chemistry* **2005**, *26*, 1701–1718.

(68) Bonomi, M.; Branduardi, D.; Bussi, G.; Camilloni, C.; Provasi, D.; Raiteri, P.; Donadio, D.; Marinelli, F.; Pietrucci, F.; Broglia, R. A.; Parrinello, M. *Computer Physics Communications* **2009**, *180*, 1961–1972.

(69) Bussi, G.; Donadio, D.; Parrinello, M. *The Journal of Chemical Physics* **2007**, *126*, 014101.

(70) Bernetti, M.; Bussi, G. *The Journal of Chemical Physics* **2020**, *153*, 114107.

(71) Essmann, U.; Perera, L.; Berkowitz, M. L.; Darden, T.; Lee, H.; Pedersen, L. G. *The Journal of Chemical Physics* **1995**, *103*, 8577–8593.

(72) Hess, B. *Journal of Chemical Theory and Computation* **2008**, *4*, 116–122.

(73) Humphrey, W.; Dalke, A.; Schulten, K. *VMD – Visual Molecular Dynamics*; manual; 1996, pp 33–38.

(74) Michaud-Agrawal, N.; Denning, E. J.; Woolf, T. B.; Beckstein, O. *Journal of Computational Chemistry* **2011**, *32*, 2319–2327.

(75) Bradshaw, R. T.; Marinelli, F.; Faraldo-Gómez, J. D.; Forrest, L. R. *Biophysical Journal* **2020**, *118*, 1649–1664.

(76) Best, R. B.; Vendruscolo, M. *Structure* **2006**, *14*, 97–106.

(77) Polyhach, Y.; Bordignon, E.; Jeschke, G. *Phys. Chem. Chem. Phys.* **2011**, *13*, 2356–2366.

Acknowledgments

Technical support for protein purifications was provided by R. Visentin, L. Falconet (Protein Platform, Faculty of Medicine, University of Geneva) and A. Cieren (Department of Physical Chemistry, University of Geneva). The mouse livers were kindly provided by Service de Zootechnie (Faculty of Medicine, University of Geneva) and the mitochondria were prepared by L.M. Epasto and A. Cieren (Department of Physical Chemistry, University of Geneva). Technical support for HDX-MS was provided by R. Visentin (Protein Platform, Faculty of Medicine, University of Geneva). EB and CE thank Prof. A.J. García-Sáez for providing the Bcl-2 plasmids and Prof. F. Marassi for providing the pdb files of full-length soluble and membrane-anchored Bcl-xL. AH and FLG thank Dr. N. Piasentin and Dr. S. Aureli for reading and commenting on the manuscript.

Funding: This work was supported by the SNSF Sinergia grant CRSII5_216587 (to EB and FLG) and partially by grant 200021_204795 (to FLG). We would like to acknowledge the CSCS for their generous allocation of supercomputing time (project : lp84).

Author contributions: CE and AH contributed equally to this work as first authors. CE, AH, OV conducted experiments and analysis. CE conducted DEER, ESEEM and protein preparations. AH conducted modelling and simulation. OV conducted HDX experiments. CE, AH, FLG and EB conceptualised and wrote the manuscript. FLG and EB acquired Funding.

Competing interests: There are no competing interests to declare.

Supplementary materials

Materials and Methods
Figs. S1 to S21
Tables S1 to S4
References *(51-77)*

Supplementary Materials for: Structural and dynamic basis of indirect apoptosis inhibition by Bcl-xL: a case study with Bid

Christina Elsner[1,†], Anton Hanke[2,3,†], Oscar Vadas[4],Francesco L. Gervasio[2,3,5,*], Enrica Bordignon[1,*]

[1]Department of Physical Chemistry, University of Geneva, 1211 Geneva, Switzerland

[2]Department of Pharmaceutical Sciences, University of Geneva, 1211 Geneva, Switzerland

[3]Swiss institute of Bioinformatics, University of Geneva, 1211 Geneva, Switzerland

[4]Department of Microbiology and Molecular Medicine, University of Geneva, 1211 Geneva, Switzerland

[5]Chemistry Department, University College London, WC1E 6BT London, United Kingdom

[*]Corresponding authors. Emails: `francesco.gervasio@unige.ch` and `enrica.bordignon@unige.ch`

[†]These authors contributed equally to this work.

This PDF file includes:

Materials and Methods
Figures S1 to S21
Tables S1 to S4

Materials and Methods

Protein expression, purification, and labeling

His-tagged mouse Bid (pET23d[53]), human Bax (pTYB1[54]), and human Bcl-xL (pTYB1[55]) were prepared as described previously[36].

In short, all plasmids except for pTYB1-Bcl-xLC23C203 (S23CC151SS203C, ordered from GenScript) were cloned by site-specific mutagenesis, which was confirmed by DNA sequencing. All proteins were expressed in *E. coli* and the proteins were purified from the soluble fraction of the bacterial lysate.

Bid was purified using Ni-NTA and washed with buffer in three steps (imidazol: 0 mM, 10 mM, 25mM) before being eluted with 250 mM imidazole. For cleavage, Bid was mixed 1:1 with cleavage buffer and cleaved with Caspase 8. Afterwards, cBid was purified with Ni-NTA.

For spin labeling with MTSL, cBid was diluted to 10-20 µM and incubated with 1 mM DTT for 1 h. After removal of DTT in a desalting column, cBid was immediately mixed with 10x excess MTSL and incubated at 8°C overnight. Excess label was removed in a desalting column.

Bax and Bcl-xL were purified using a chitin resin and washed thoroughly before cleaving the intein tag off overnight by incubation with DTT. After elution, Bcl-xL was dialyzed in one step 1:10 against 20 mM Tris (pH 8.0) and Bax was dialyzed in five steps against 8 mM Tris (pH 8.0). Both proteins were further purified using anion exchange columns. For Bcl-xL 1 mM DTT was added to the buffers forloading, washing, and elution.

The pooled fractions of Bcl-xL were purified in a third step using a Superdex 200 10/300. If the protein had to be labeled, 10 μM TCEP was added to the buffers.

MTSL-labeling of Bax and Bcl-xL was performed with protein concentrations between 10 and 20 μM and 5-10x excess of MTSL at 8°C overnight. The excess label was then removed by washing in centrifugal filters.

All proteins were tested in pore formation assays (see Fig. S2) before further experimental use.

LUVs preparation

Large unilamellar vesicles (LUVs) for EPR, HDX and pore formations assays were prepared as described before[36] with a composition mimicking the MOM (46% egg L-α-phosphatidyl choline (PC), 25% egg L-α phosphatidyl ethanolamine (PE), 11% bovine liver L-α-phosphatidyl inositol (PI), 10% 18:1 phosphatidyl serine (PS) and 8% cardiolipin (CL) (% w/w)). In short, the dried lipid mixture was resuspended either in storage buffer (EPR,

HDX) or in calcein solutions (80 mM, pore formation assays) and extruded through a membrane with 400 nm pores. As control, a lipid mixture corresponding to the exact composition used in the MD simulations was prepared the same way with 80% 1-palmitoyl-2-oleoyl-sn-*glycero*-3-phosphocholine (POPC) and 20% CL.

Pore formation assays

The pore formation assays were performed as decribed before [36]. In short, the calcein was trapped in the LUVs at a high, self-quenching concentration, leading to a low fluorescence intensity. Upon pore formation in the membrane, calcein is diluted in the surrounding buffer leading to increasing fluorescence intensity. All proteins were used at 25 nM final concentration.

Continuous wave EPR

Room temperature CW EPR experiments were performed on a Bruker E500 X-band equipped with a super high Q cavity ER 4122 SHQ with a power of 2 mW and a modulation amplitude of 0.1 or 0.15 mT. Samples were measured in glass capillaries (Blaubrand). Spin counting was performed by comparison of the second integral of the EPR spectrum with the second integral of a reference spectrum of a 100 μM TEMPOL solution in water.

Pulsed EPR measurements

All pulsed EPR experiments were performed at 50 K on a Bruker Q-band Elexsys E580 spectrometer equipped with a 150 W TWT amplifier, a Bruker Spinjet-AWG, and a home-made probe head accommodating 3 mm o.d. tubes.

Here, we used the dead-time free 4-pulse DEER sequence with Gaussian pulses [56] (predefined pulse shape in Bruker Xepr version 2.6b.170) and 16-step phase cycling. All pulses were adjusted to the same pulse length (36 ns corresponding to 16-20 ns FWHM) with the pump position at the maximum of the nitroxide spectrum and the observer at -90 MHz. The upper limit of accurate mean distances (shaded region in all DEER distance distributions shown in the figures) was calculated by [42]:

$$r_{max} \approx 5 \cdot \sqrt[3]{\frac{t_{max}}{2\mu s}} nm \tag{S1}$$

table S2 summarizes the used parameters.

For ESEEM we used the 3-pulse sequence with rectangular 12 ns pulses and 4-step phase cycling to eliminate running echoes. τ was optimized in 2D 3-pulse ESEEM experiments to

maximize the deuterium signals. Parameters are summarized in table S3.

Solution samples for DEER were prepared by mixing 20 μl protein sample with 20 μl d8-glycerol. Membrane samples were prepared by incubating the protein mixtures with LUVs for 1 h at 37°C and by separating the pellet from the supernatant by centrifugation. The pellet was resuspended in buffer prepared with deuterated water and mixed with 10% d8-glycerol to the final sample volume of 40 µl. The samples were shock frozen in 3 mm o.d. quartz tubes (Aachener Quarzglas) and stored at -80°C.
DEER data were analyzed with DeerAnalysis [57] 2022 using Tikhonov regularization. ESEEM data were analyzed within the Bruker Xepr software by fitting the trace with a biexponential decay and dividing the data by the fit for baseline correction. After application of a Hamming function and zero filling, the data were Fourier transformed to obtain the intensity of the deuterium signals used as descriptors of the water accessibility of teh spin-labeled side chain.

Hydrogen/deuterium exchange mass spectrometry

HDX-MS experiments were performed at the UniGe Protein Biochemistry Platform (University of Geneva, Switzerland) following a well-established protocol with minimal modifications [58]. The following conditions were tested and compared: i) Bcl-xL; ii) Bcl-xL + LUVs; iii) Bcl-xL + LUVs + cBid and iv) cBid. For Bxl-xL and cBid, a first concentrated mix was prepared and preincubated for 5 min at the reaction temperature before initiating deuteration reaction. For reactions containing LUVs (conditions ii and iii), proteins (340 pmol) were pre-incubated with LUVs for 1h at 37 °C. The mix was then centrifuged at 20'000 ×g for 30 min at 22 °C and the supernatant containing proteins unbound to lipids was removed. The pelleted material was used for deuterium labelling.

Deuterium exchange reaction was initiated by adding deuterated buffer at the defined temperature to a final reaction volume of 50 microliters. Reactions were carried-out for defined times and terminated by the sequential addition of ice-cold quench buffer. Samples were immediately frozen in liquid nitrogen and stored at -80 °C for up to two weeks.

To quantify deuterium uptake into the protein, samples were thawed and injected in a UPLC system immersed in ice with 0.1 % FA as liquid phase. The protein was digested via an immobilized Nepenthesin-2/Pepsin mixed column (AffiPro AP-PC-006), and peptides were collected onto a Nucleodur 300-5 C18 pre-column filter (Macherey-Nagel). The trap was subsequently eluted, and peptides separated with a C18, 175 Å, 1.9 μm particle size Thermo Hypersil Gold Vanquish 100 x 2.1 mm column over a gradient of 8 – 30 % buffer C over 20 min at 150 μl/min (Buffer B: 0.1% formic acid; buffer C: 100% acetonitrile). Mass spectra were acquired on an Orbitrap Velos Pro (Thermo), for ions from 400 to 2200

m/z using an electrospray ionization source operated at 300 °C, 5 kV of ion spray voltage. Peptides were identified by data-dependent acquisition of a non-deuterated sample after MS/MS and data were analyzed by Mascot 2.6 using a database composed of purified proteins and known contaminants. Precursor mass tolerance was set to 10 ppm and fragment mass tolerance to 0.6 Da. Protein digestion was set as nonspecific. All peptides analysed are shown in HDX Tables. Deuterium incorporation levels were quantified using HD examiner version 3.4.2 software (Sierra Analytics), and quality of every peptide was checked manually. Results are presented as percentage of maximal deuteration compared to theoretical maximal deuteration. Criteria to define changes in deuteration level between two states as significant are indicated in the tables.

Mitochondria purification

Crude mitochondria were isolated from mouse liver as described in literature[59]. In short, fresh mouse livers with a total of approximately 3.2 g were cut in small pieces on ice and homogenized in sucrose buffer using a glass dounce homogenizer. The homogenate was centrifuged at $600\times g$ for 10 minutes at 4°C to remove any cell debris. Subsequentially, the supernatant was centrifuged at $7000\times g$ for 10 minutes at 4°C. Approximately 1 mL of crude mitochondria suspension in sucrose buffer was then obtained and kept on ice. Mitochondrial proteins were considered as an index of mitochondrial concentration, and they were determined using a Bradford assay. The final protein concentration was around 90 mg/mL.

For DEER samples mitochondria (final amount: ~ 1 mg mitochondrial protein) were mixed with proteins (final amount: ~ 0.5 nmol) and incubated for 5 min at 37°C. Then they were centrifuged for 3 min at 7000×g and 4°C. The supernatant was removed and the mitochondria were resuspended in 30 μl deuterated Threalose buffer (200 mM Trehalose, 10 mM HEPES, 10 mM EGTA, 10 mM EDTA) to the final sample volume of 40 µl. The samples were shock frozen in 3 mm o.d. quartz tubes (Aachener Quarzglas).

Model generation

Hetero-complex models were based on a model of membrane-associated Bcl-xL by Ryzhov et al. [8], PDBid 2m5i [35] and PDBid 4qve [21]. As such the model comprised human Bcl-xL and tBid. Models of the hetero-complex were generated with custom modelling classes within the Modeller python software package [40]. Input reference PDB structures for Modeller [40] were prepared as follows:

1. The BH3 helix and N-terminal loop was removed from all models within PDB 2m5i [35].

2. From the apo Bcl-xL model the loop connecting helix $\alpha 8$ to $\alpha 9$ was removed.

3. Modified apo Bcl-xL model was aligned to the Bcl-xL chain in PDB 4qve [21].

4. Modified 2m5i structures were positioned such that the N-terminal is close to the C-terminal of the BidBH3 in 4qve and parallel to the membrane plane of the modified apo Bcl-xL model, such that the membrane interacting residues point towards the membrane [8, 35].

Alignments and placements were made with PyMOL [60]. Models were generated using the LoopModel class of Modeller with the following additional restraints: (i) Bcl-xL was rigid body restrained except in the $\alpha 1/2$ loop and after helix $\alpha 8$, (ii) Alpha helices $\alpha 9$ of Bcl-xL, $\alpha 4$, and $\alpha 5$ of tBid were secondary structure restrained, (iii) the centre of mass distance between DEER residue pairs were restrained to the global maximum of the DEER probability distributions with the Gaussian restraint form in Modeller and a standard deviation of 0.5 Å, and (iv) the z positions of atoms in the tBid N-terminal loop were lower bound restraint to be above the membrane plane implied by the modified apo Bcl-xL model. Only the beginning of the Bcl-xL $\alpha 1/2$ loop (residues 21 to 27) and tBid N-terminal loop were selected during loop remodelling. Initial modelling used the autoscheduler with maximum 600 conjugate gradient iterations, no MD refinement and 14 optimization repeats. Loop modeling used the fast MD refinement and ten optimization repeats. Models were discarded if their molpdf score was above 2×10^{10}. Generated output models were re-scored based on their DOPEHR score and a DEER score as per the following:

$$S_{mdl} = \text{DEER score} + \ln\left(\text{DOPEHR} - \min_{mdls}(\text{DOPEHR}) + 1.0\right) \tag{S2}$$

The DEER score of a model is computed as the sum of all Wasserstein distances between normalised[1] experimental DEER distance distributions and their corresponding estimated distributions in the model. DEER distributions of distances in the models were estimated using DEER-PREdict [41, 61]. Briefly, DEER-PREdict places a rotamer library of the DEER label onto the distance partners, removing clashing rotamers and calculates the distance distribution between the paired electrons. Models were protonated at pH 7.5 using pdb2pqr [62] and propka [63] giving a total charge of $-9e$ to the hetero-complex.

Molecular Dynamics simulations

The protonated highest scoring Bcl-xL/tBid (holo) model was solvated with CHARMM-GUI [64] in a hexagonal box containing 576 (80 %) POPC and 144 (20 %) 9,10 and 12,13 unsaturated cardiolipin (TLCL) (charge: $-2e$). This membrane composition was tested for

[1] such that $\int P(d) = 1.0$

Bcl-xL activity and complex formation in the experimental setup and showed comparable distance distributions to other conditions (see Fig. S17). Lipids were equally distributed across the leaflets and the system solvated in TIP3P water [65]. The box was charge neutralised with sodium chloride and sodium chloride atoms added to a $150\,mM$ concentration. Within the box the protein was positioned such that tBid is slightly above the membrane plane to allow for proper lipid placement by CHARMM-GUI.

After energy minimization and equilibration tBid was embedded into the membrane using adaptive biasing MD [66]. Embedding was described by the minimum value of the difference in coordination of each hydrophobic residue in tBid with lipid phosphates and carbons. The secondary structure of tBid was restrained by the sum of all backbone hydrogen bonds in alpha helices. Once reasonable embedding was achieved, adaptive biasing MD simulations were stopped. Embedding was followed by a $15\,ns$ relaxation in which only the secondary structure of tBid and the lipid phosphate positions were restrained. Phosphates were restrained towards the mean value in the z-dimension of the initial frame shifted towards tBid by 0.5 Å and secondary structure restrained as before. For restraint strengths see Table S4. For production simulations the equilibrated and embedded system was copied seven times to run seven independent replicates. First $60\,ns$ of unrestrained MD were run with new initial velocities and discarded as equilibration, to which followed seven production simulations. Each production replicate has a duration of $1\,\mu s$.

Bcl-xL only (apo) systems were generated with CHARMM-GUI from the Bcl-xL apo model [8]. The protein was embedded in 20 % TLCL and 80 % POPC at $150\,mM$ NaCl and neutralising ions. Four independent replicates were equilibrated from the generated system (see Table S4), followed by $200\,ns$ of production simulation.

All simulations were run with GROMACS 2023 [67] and plumed 2.9.0 [68]. For water the modified charmm36m water parameters were used and for lipids, ions, and protein the charmm36m forcefield was used [65]. A breakdown of changing simulation settings throughout the equilibration and production simulations can be found at Table S4.In NVT and NPT simulations the V-rescale thermostat was employed at a temperature of $310.15\,K$ at a time constant of $1.0\,ps$, separately coupling membrane, protein and solvent [69]. NPT simulations used a semi-isotropic C-rescale barostat [70] at $1\,atm$ with a compressibility of $4.5e-5\,bar^{-1}$ and a time constant of $5.0\,ps$. Neighbour lists were build with the Verlet cutoff scheme. Lennard-Jones interactions were treated with the Cut-off scheme using force-switching at $1.2\,nm$ and switch radius of $1.0\,nm$. Coulomb interactions were calculated using particle-mesh-ewald [71] with a cutoff $1.2\,nm$. Hydrogen bonds were LINCS [72] constrained and center of mass motion removed every 100 steps on the solvent and solute groups separately. Frames were written to trajectory at a frequency of $10\,\frac{1}{ns}$.

Molecular Dynamics analysis

Production simulations were analysed visually with VMD and pymol [60, 73]. Root mean squared deviation (RMSD), root mean squared fluctuation (RMSF), atom based principle component analysis (PCA), solvent accessible surface area (SASA), angles and distances were calculated using GROMACS tools and MDanalysis [74]. Unless specified otherwise, trajectories were analysed at an interval of $1\,\frac{1}{ns}$. Both for RMSF and atom based PCA analysis simulations were aligned to the first frame of the simulation based on the Cα-atoms of helices $\alpha5$ and $\alpha6$ and analysed at $10\,\frac{1}{ns}$. The PCA aligned trajectory was also used to compute the dynamic cross-correlation matrix of Cα-atom displacement of protein residues.

DEER distributions within production simulations were calculated using DEER-PREdict [41] (see: equation S2) for each frame in the trajectories ($10\,\frac{1}{ns}$). Total distributions were obtained by summing the distributions of separate trajectories and normalising by $\int P(d)$.

HDX deuteration levels in simulations were calculated following Best and Vendrusculo [75, 76] using HDXer[2]. Simulations were analysed with the method of Best and Vendruscolo [76] at deuteration times of $0.05/0.5/5.0\,min$, $22°C$, at pH 7.5 and maximum deuteration fraction of 90.4 %.

Contact maps and probabilities were calculated using custom wrapper modules around MDAnalysis [74] defining a contact as a distance lower than $0.7\,nm$ between the relevant heavy side-chain atom center of mass (CoM) of two residues. Independently moving domains within the hetero-complex were identified via the standard deviation matrix of distances between the centres of mass of all protein residue sidechains. Membrane contacts were calculated at $0.5\frac{1}{ns}$. Binding site dynamics were compared by calculating the distance between the centre of mass of the backbone of residues 107 to 112 and 137 to 141 in Bcl-xL. The angle of the binding site in relation to the membrane was calculated as the angle between the z-axis and the vector between the $C\alpha$ atoms of A104 and E129. Calculations were done for both apo and holo simulations.

To obtain an overview over loop and general dynamics of the complex a PCA was calculated for the distance matrix between Bcl-xL and tBid using the same selections as for the contact maps (see Fig. S11). The PCA explained 90 % of cumulative variance in the distance matrix between Bcl-xL and tBid and was consecutively clustered first by OPTICS and then by KMeans to obtain the number of clusters and assign a state to all considered frames. Clusters were sorted by size.

All structural images were rendered with PyMOL [60] or Molecular Nodes[3] in Blender.

[2] `https://github.com/Lucy-Forrest-Lab/HDXer`
[3] `https://github.com/BradyAJohnston/MolecularNodes`

Biological graphics were supplemented with visual's obtained from BioRender[4].

[4] https://www.biorender.com/

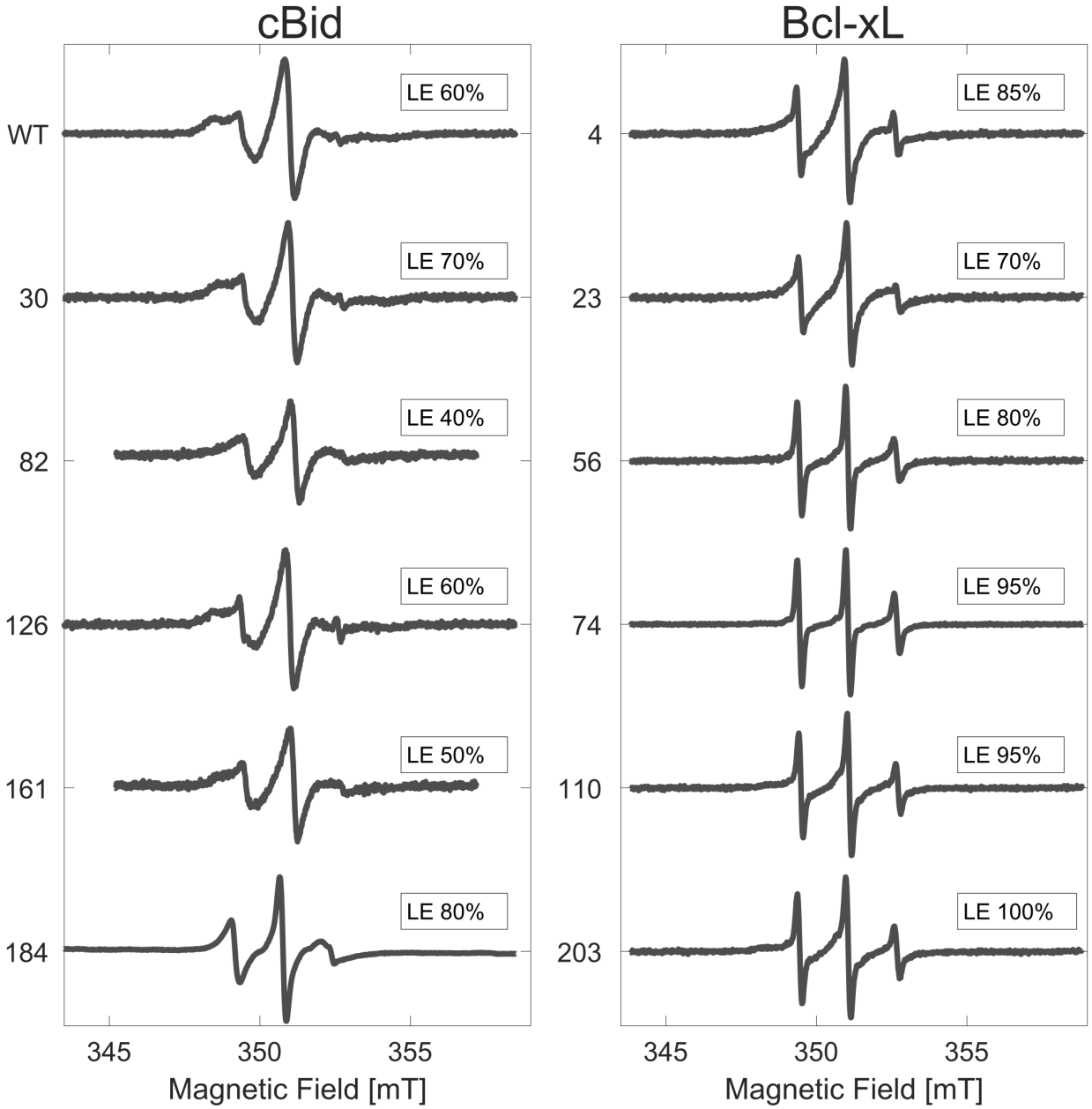

Figure S1: Room temperature continuous wave EPR spectra of spin-labeled cBid and Bcl-xL variants. The wild type cBid (WT) contains two natural cysteines (C30 and C126) which were both spin labeled. The other cBid variants are singly spin-labeled at the indicated cysteine positions (one or two natural cysteines were replaced by serines). The Bcl-xL variants are singly spin-labeled at the indicated cysteine positions (the natural cysteine C151 was replaced by serine). Labeling efficiencies (LE, spin per cysteine, 10% error) were determined by comparing the second integral of the spectra with the spectrum of TEMPOL in water with known concentration.

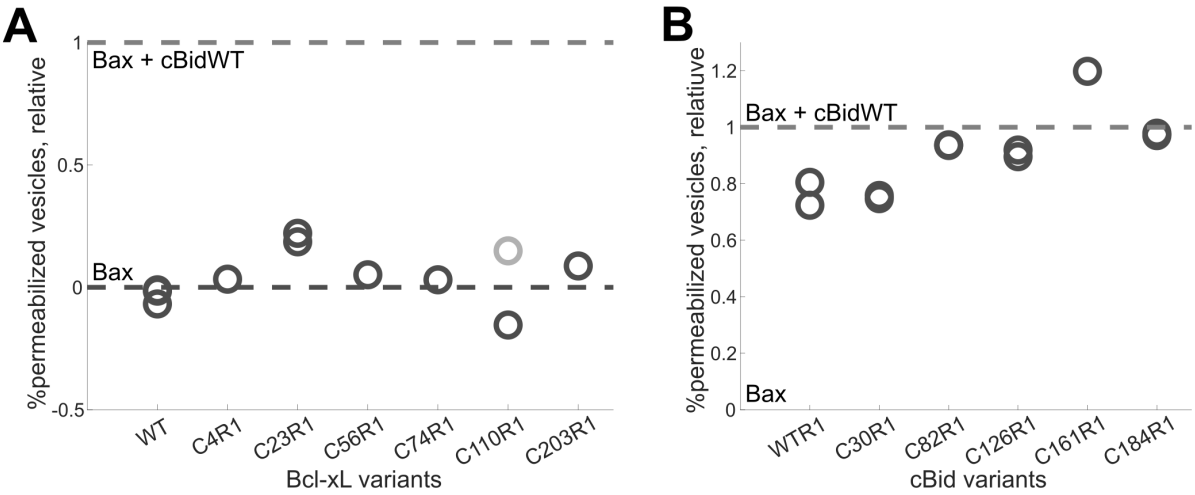

Figure S2: Activity of spin-labeled Bcl-xL and cBid variants by pore-formation assays. Comparison of the release of calcein from LUVs for different Bcl-xL **(A)** and cBid **(B)** spin-labeled variants after 30 min incubation. **(A)** Activity of Bcl-xL variants in presence of Bax and cBid (25 nM concentrations 1:1:1 protein ratio). To facilitate the comparison of the inhibitory effects of Bcl-xL variants with different LUVs batches, data were normalized as follows: zero is the calcein release with Bax alone (Bax autoactivity) and one the maximum release obtained with Bax and cBidWT. All spin-labeled variants are shown to inhibit membrane permeabilization. **(B)** Activity of cBid variants in presence of Bax (25 nM concentrations 1:1 protein ratio). Normalization as in panel A.

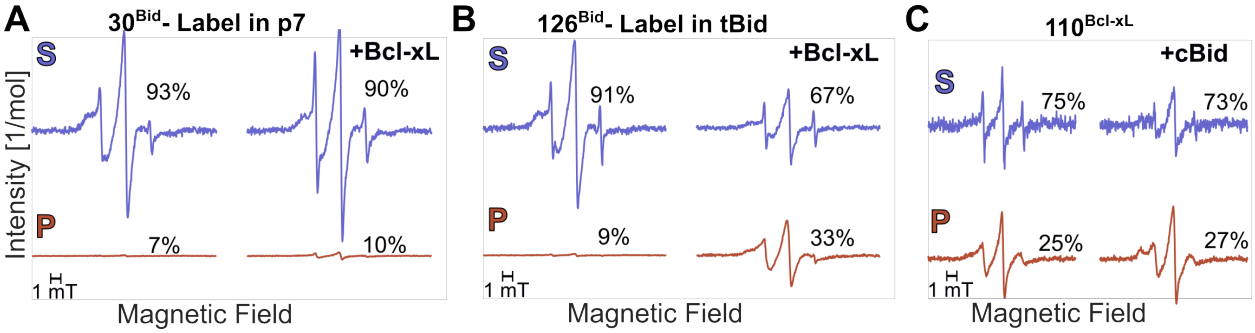

Figure S3: Membrane-water partitioning of spin-labeled cBid and Bcl-xL variants. Room temperature continuous wave EPR spectra of spin-labeled cBid and Bcl-xL variants were recorded in the supernatant (S) and pellet (P) fractions after incubation. The number of moles of p7 **(A)**, tBid **(B)** and Bcl-xL **(C)** in each fraction was calculated based on the spectral area (spin concentration) and the volume of each fraction. The spectra are normalized by the number of moles in each fraction and the relative amount is shown in percentage (the estimated error is 10%), presented in fig. 2B

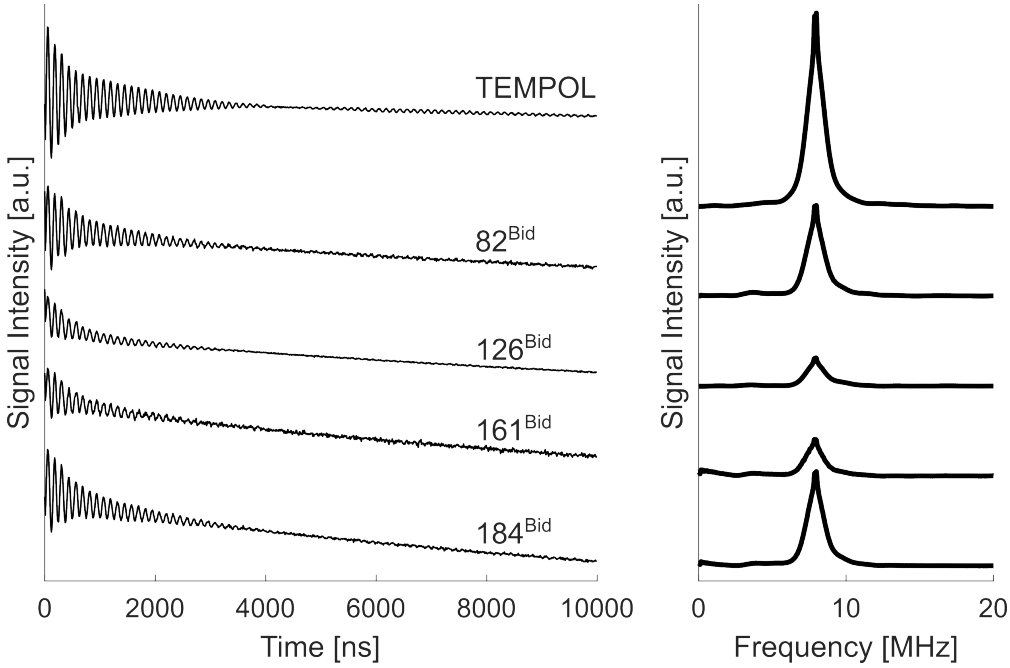

Figure S4: 3-pulse ESEEM data of spin-labeled cBid in presence of unlabeled Bcl-xL in pellet fractions. Pellets were resuspended with deuterated buffer and 10% d_8-glycerol. Left: Raw data of Fig. 2C normalized by the number of scans. Right: Deuterium signal intensity after Fourier transformation, presented in fig. 2C (the estimated error based on technical repeats is 10%). The reference sample was prepared by adding TEMPOL after pellet resuspension.

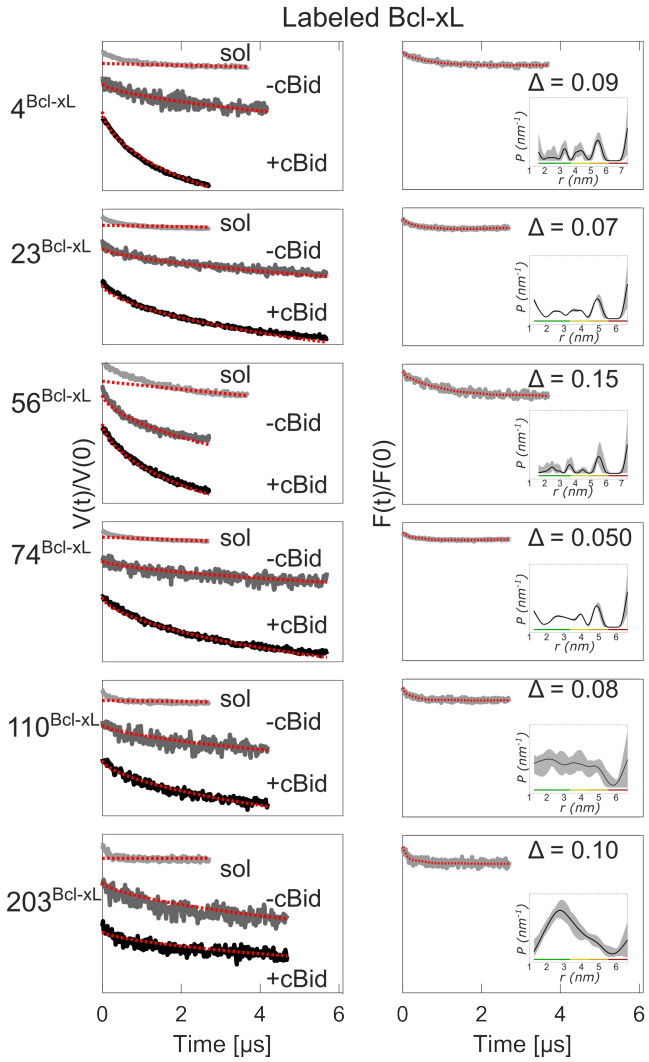

Figure S5: DEER analysis of singly-labeled Bcl-xL variants in solution (sol) and in LUVs without cBid wt (-cBid), and in LUVs with unlabeled cBid wt (+cBid). Left panels: Primary data (grey and black) and 3D background fit (dotted red, for the samples in solution - sol-) or 2D background fit (dotted red, for the membrane samples -cBid and +cBid). The 2D-background (starting at the zero time point) is almost indistinguishable from the DEER primary traces in membranes, indicating that Bcl-xL does not form defined dimers or higher order oligomers. The background is often steeper when adding cBid which might indicate higher molecular crowding when tBid is bound to Bcl-xL at the membrane. Right panels: Form factor of the solution samples obtained after dividing the primary data by the background (grey), fit (red dotted) and corresponding modulation depth (Δ). The insets show the resulting distance distributions obtained with Tikhonov regularization. the low modulation depth and the broad distributions are characteristic of residual Bcl-xL/Bcl-xL aggregates in solution.

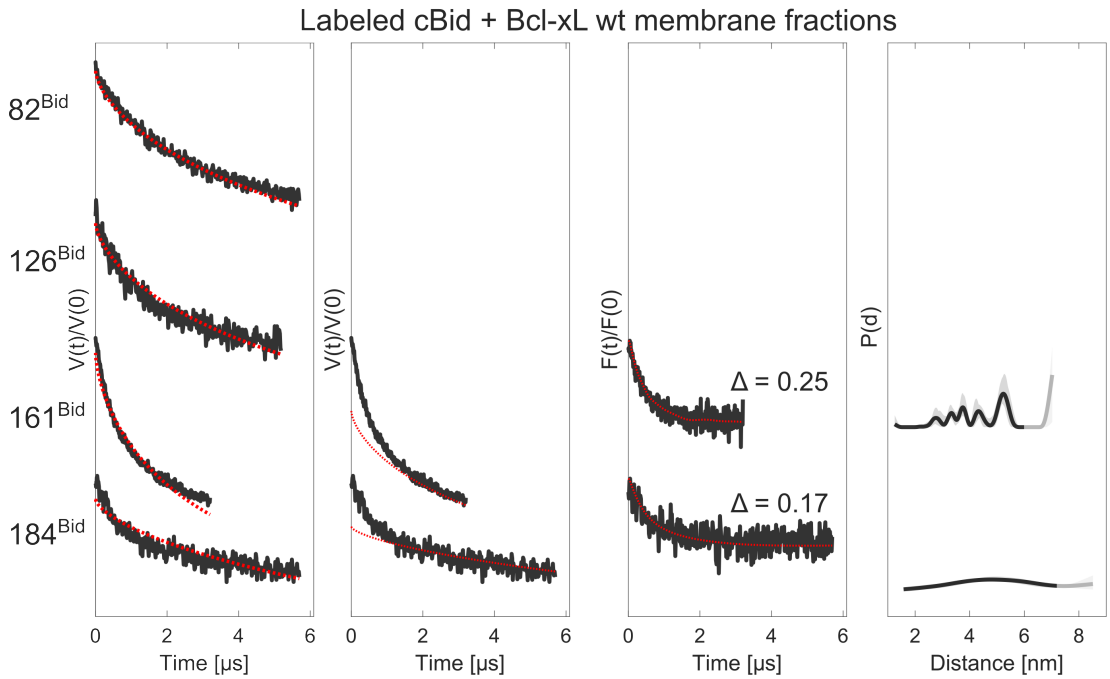

Figure S6: DEER analysis of singly-labeled cBid variants in LUVs unlabeled Bcl-xL wt. From left to right: Primary data (black) with a 2D background fit (dotted red) starting from zero; the same primary data of two traces with a 2D background starting at 2 microseconds (dotted red); Form factor obtained after dividing the primary data by the background (black), fit (red dotted) and corresponding modulation depth (Δ); resulting distance distributions obtained with Tikhonov regularization with uncertainties (shaded grey areas) derived by varying the starting point of the background fit and the noise level. The comparison of the traces with a decay caused only by the two dimensional distribution of the spin-labeled proteins highlights that the traces are almost indistinguishable from a 2D background, indicating that there are no specific cBid/cBid interactions at the membrane when the inhibitory complex is formed. For positions 161 and 184 the traces deviate more from from a 2D background. The fit with a 2D background starting at 2 microsecond demonstrate that aspecific interaction are detected, indicating molecular crowding at the membrane of the C-terminal region of cBid.

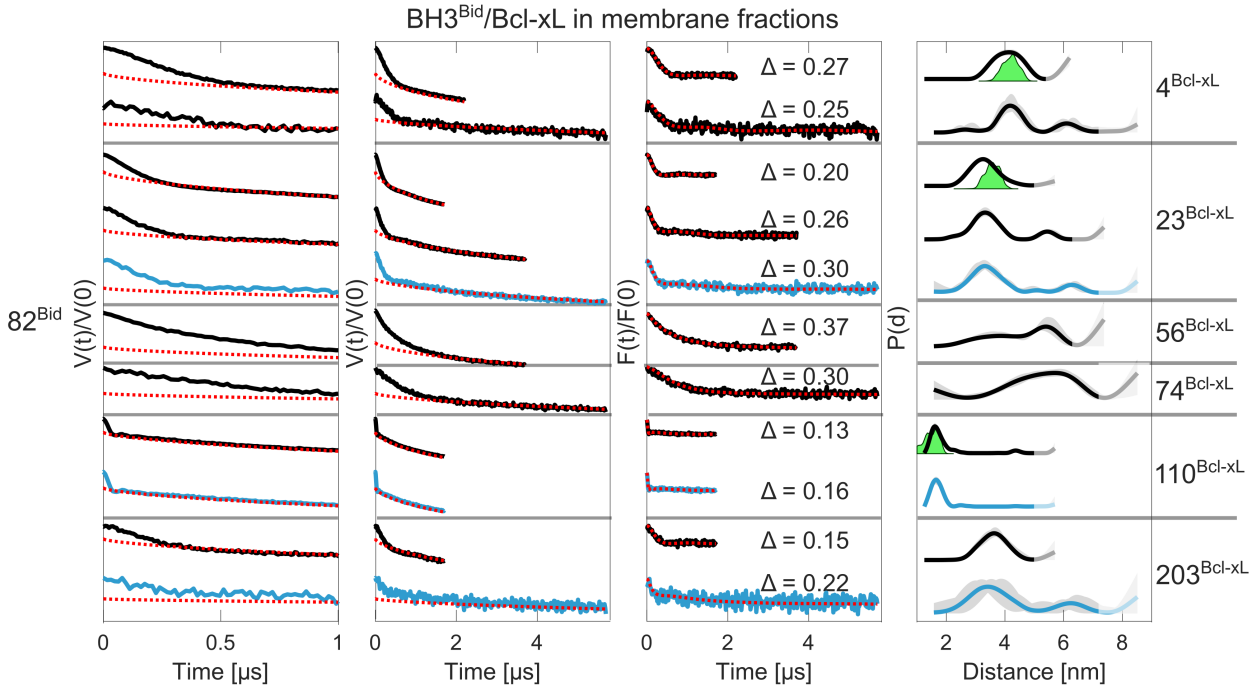

Figure S7: BH3^{Bid}/Bcl-xL distance measurements in membranes (part I). From left to right: One microsecond zoom on the primary DEER data (black) with a 2D background fit (dotted red); primary DEER data (black) with a 2D background fit (dotted red); the same primary data of two traces with a 2D background starting at 2 microseconds (dotted red); Form factor obtained after dividing the primary data by the background (black), fit (red dotted) and corresponding modulation depth (Δ); resulting distance distributions obtained with Tikhonov regularization with uncertainties (shaded grey areas) derived by varying the starting point of the background fit and the noise level. Technical and biological repeats are shown. The traces are shaded to highlight the distance range in which the accuracy is not adequate, due to the maximal length of the trace detected. The blue traces are those used as first three constraints to create the initial model in Fig. 3. The three green areas represent the three distance distributions which can be predicted with MMM[77] on the crystal structure of the water-soluble truncated Bcl-xL in complex with a Bid-derived BH3 peptide (PDB: 4QVE). The predicted distributions are in very good agreement with the distributions obtained with the full-length Bcl-xL and cBid at the membrane, confirming the presence of the same BH3-into-groove interaction.

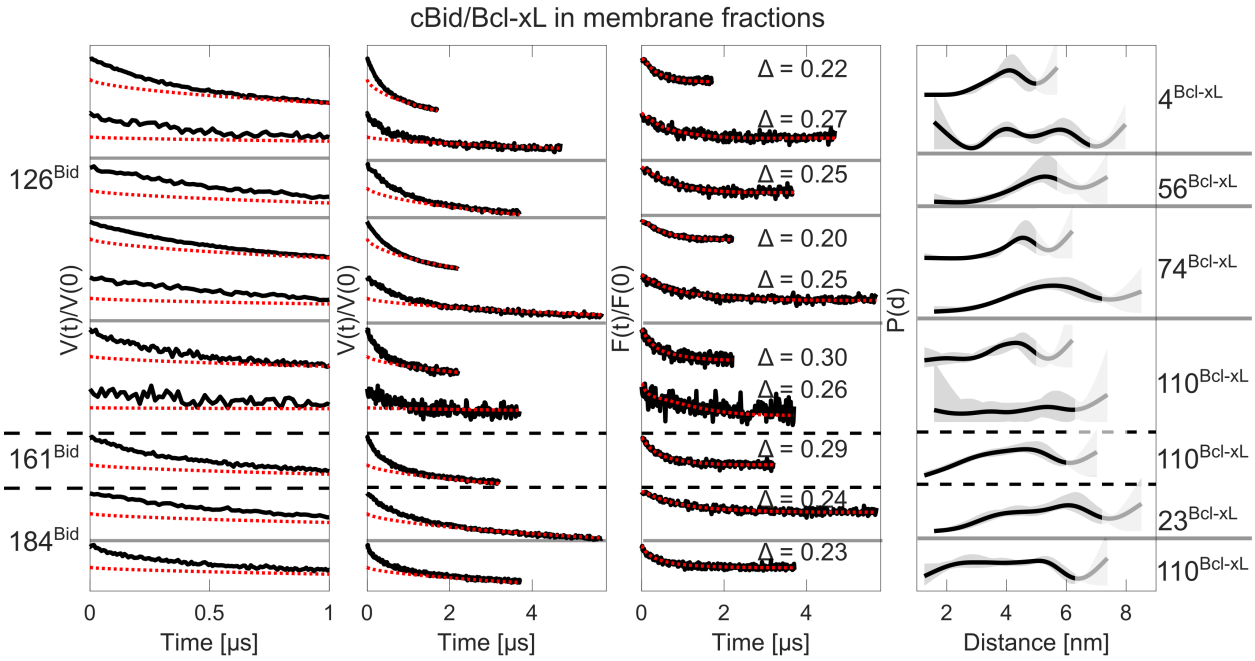

Figure S8: cBid/Bcl-xL distance measurements in membranes (part II). From left to right: One microsecond zoom on the primary DEER data (black) with a 2D background fit (dotted red) ; primary DEER data (black) with a 2D background fit (dotted red); the same primary data of two traces with a 2D background starting at 2 microseconds (dotted red); Form factor obtained after dividing the primary data by the background (black), fit (red dotted) and corresponding modulation depth (Δ); resulting distance distributions obtained with Tikhonov regularization with uncertainties (shaded grey areas) derived by varying the starting point of the background fit and the noise level. The traces are shaded to highlight the distance range in which the accuracy is not adequate, due to the maximal length of the trace detected. For the same sample, traces of different lengths are shown as technical repeats.

```
E-value: 1e-73  Identity: 126/198
Cleave site indicated by: xxxx (cleaved after last x)
                                                                    xx
Human   MDCEVNNGSSLRDECITNLLVFGFLQSCSDNSFRRELDALGHELPVLAPQWEG--YDELQ
Mouse   MDSEVSNGSGLGAEHITDLLVFGFLQSSG--CTRQELEVLGRELPVQA-YWEADLEDELQ
        **.**.***.*  * **:*********..  . *:**:.**:**** *  **.   ****
        xx
Human   TDGNRSSHSR-LGRIEADSESQEDIIRNIARHLAQVGDSMDRSIPPGLVNGLALQLRNTS
Mouse   TDGSQASRSFNQGRIEPDSESQEEIIHNIARHLAQIGDEMDHNIQPTLVRQLAAQFMNGS
        ***.::*:*   ****.******:**:********:**.**:.* * **. ** *: * *

Human   RSEEDRNRDLATALEQLLQAYPRDMEKEKTMLVLALLLAKKVASHTPSLLRDVFHTTVNF
Mouse   LSEEDKRNCLAKALDEVKTAFPRDMENDKAMLIMTMLLAKKVASHAPSLLRDVFHTTVNF
         ****:.. **.**:::  *:*****::*:**::::*********:**************

Human   INQNLRTYVRSLARNGMD    " ": different
Mouse   INQNLFSYVRNLVRNEMD    ".": similar residue
        ***** :***.*.** **    ":": highly similar residue
```

Figure S9: Sequence alignment of human and mouse Bid. Human tBid was used for the modeling, mouse cBid was used for the EPR and HDX-MS experimental data. The cleavage occurs at the end of the sequence LQTD (indicated with `xxxx`), with D being at position 59 for mouse and 60 for human Bid. The N-terminal fragment of cBid is called p7 (7 kDa) and the C-terminal fragment tBid (15 kDa). Alignment generated with clustalw.

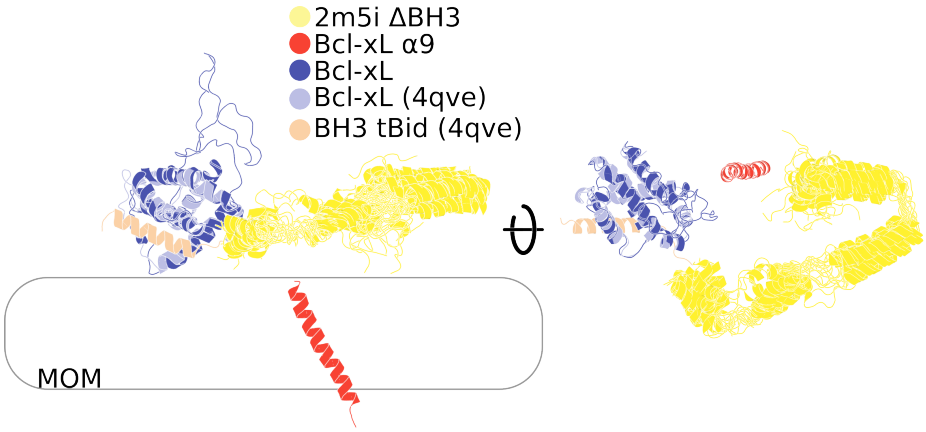

Figure S10: Positioning of input structures for Modeller shown as cartoon.

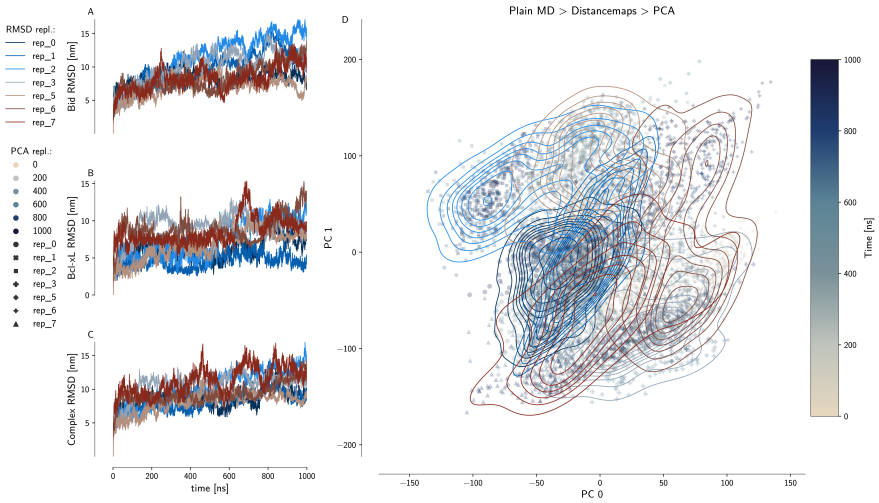

Figure S11: RMSD and PCA of MD simulations. (A-C) RMSD of independent simulation replicates over time, decomposed into the Complex (C) and its components (A, B). (D) Scatter and density plot of the independent simulation replicates within the two first principle components of distances between Bcl-xL and tBid $C\alpha$-atoms.

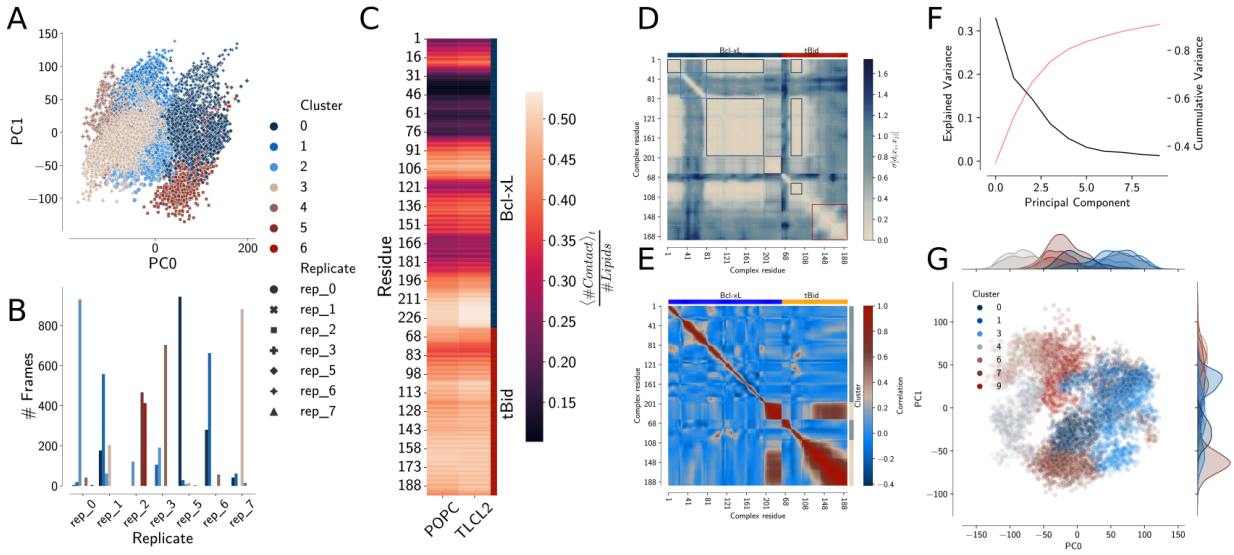

Figure S12: Supplementary materials for Fig. 4. (A) Gaussian mixture model based clustering of distances between Bcl-xL and tBid mapped onto the first two principal components (see methods). **(B)** Decomposition of clusters and their sizes over the different independent simulation replicates. **(C)** Contact frequency of each residue in Bcl-xL and tBid with either POPC or Cardiolipin (TLCL2). **(D)** Standard deviation matrix of protein residue residue distances, the identification of the different clusters (squares with the same color) is guided by biological intuition. **(E)** Dynamic cross-correlation matrix of residue displacement (blue to red) clustered by agglomerative clustering (right heatmap margin; gray and beige) with the cluster number chosen based on the highest silhouette score (~ 0.44). This clustering identifies separately the membrane and water diffusing parts of the complex, composed of the Bcl-xL TMD and C-terminal helices of tBid, or the globular Bcl-xL domain, $\alpha 1/2$ loop and tBids BH3 helix respectively. **(F)** Explained variance by each principal component of the $\alpha 1/2$ loop CA-atom displacement. **(G)** Scatter plot of the $\alpha 1/2$ loop CA-atom displacement within the first two principal components clustered within PC space by Gaussian mixture.

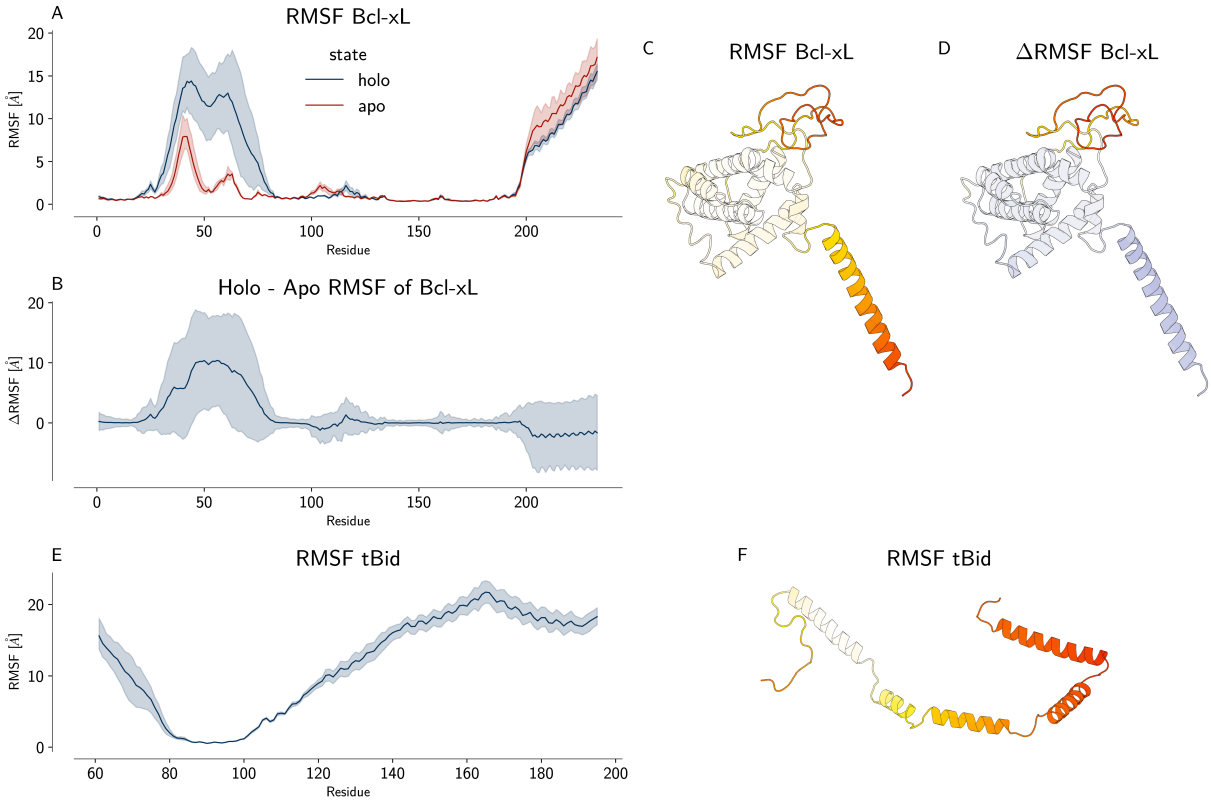

Figure S13: Binding of tBid to Bcl-xL increases Bcl-xL's flexibility. **(A)** RMSF comparison of the apo and holo simulations of Bcl-xL. **(B)** ΔRMSF of apo and holo Bcl-xL. **(C)** Cartoon representation of Bcl-xL with the holo RMSF mapped (low: white; high:red) onto the structure, note the highest RMSF is in the $\alpha 1/2$ loop and $\alpha 9$ (trans membrane domain). **(D)** Cartoon representation of Bcl-xL with the ΔRMSF mapped (negative: blue; low: white; positive: red) onto the structure. The highest impact of binding onto Bcl-xL flexibility is in the $\alpha 1/2$ loop. **(E)** RMSF of tBid in the hetero-complex. **(F)** Cartoon representation of tBid on the membrane colored by RMSF (low: white; high: red), note that the BH3 domain of tBid is rigidly bound to the globular domain of Bcl-xL. RMSF values were calculated by aligning all simulations to the residues 54 to 195 within Bcl-xL in their first frame.

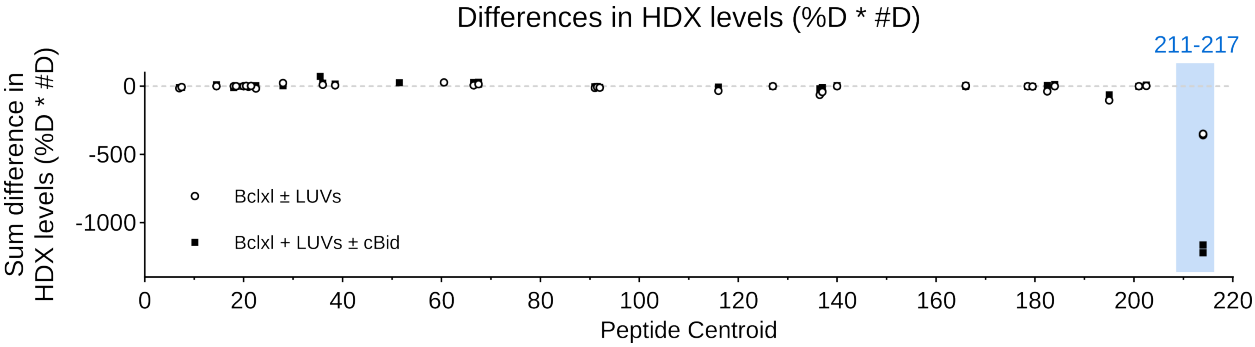

Figure S14: Differences in deuteration levels of Bcl-xL: Comparison of deuterium incorporation for each studied peptide is represented. The sum of differences for all timepoints is calculated, both as percentage deuteration ($\%D$) and number of deuterons ($\#D$). The product of the sum in differences in $\%D$ and $\#D$ is then multiplied to increase signal-to-noise ratio. Regions highlighted in blue indicate protection from exchange by the ligand. White circles: Bcl-xL in LUVs compared to Bcl-xL in solution. Black squares: Bcl-xL in LUVs with cBid compared to Bcl-xL alone in LUVs.

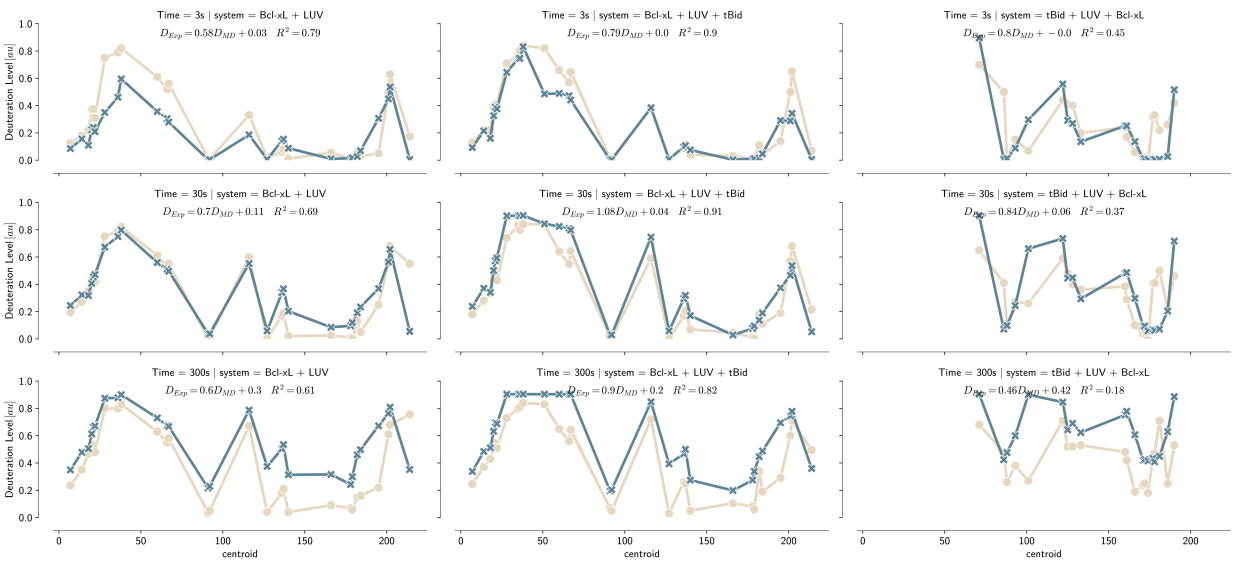

Figure S15: Deuteration levels for both Bcl-xL and Bcl-xL/tBid on LUV's. Comparison between experimental measurements (Bcl-xL + mouse cBid) and MD simulations (Bcl-xL + human tBid). R^2 and linear equations are obtained by linear regression of the experimental against the MD simulation deuteration factors.

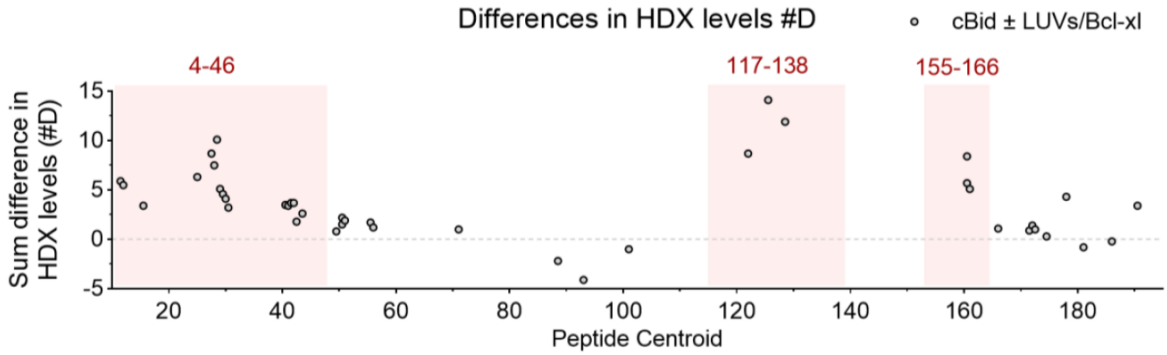

Figure S16: Comparison of the deuterium incorporation for each studied peptide of cBid in the pellet fraction (cBid mixed with Bcl-xL and LUVs) versus cBid alone in solution. The sum of differences (pellet minus solution) for all time points is calculated, both as percentage deuteration ($\%D$) and number of deuterons ($\#D$). The product of the sum in differences in $\%D$ and $\#D$ is then multiplied to increase signal-to-noise ratio. Regions highlighted in red have a higher deuterium exchange going from the soluble cBid to the membrane-associated complex. cBid is cleaved by caspase 8 after Asp 60 in mouse Bid.

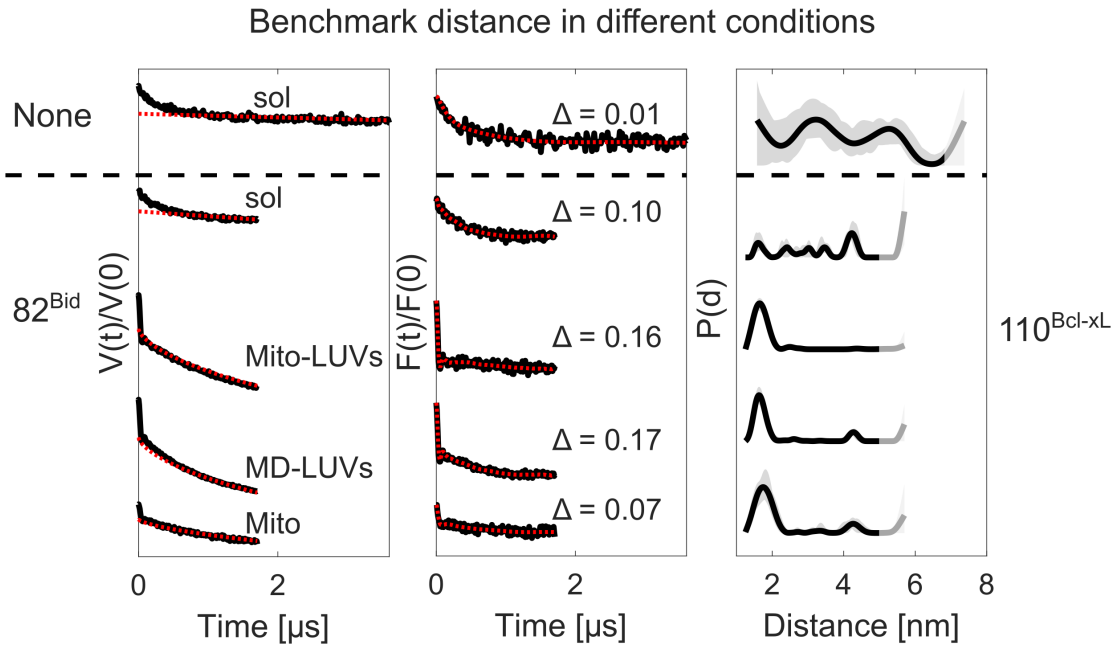

Figure S17: Benchmark $82^{\text{Bid}}/110^{\text{Bcl-xL}}$ distance measurements in different conditions. From left to right: Primary DEER data (black) with 3D- (for solution samples) or 2D-background fit (red dotted); Form factor obtained after dividing the primary data by the background (black), fit (red dotted) and corresponding modulation depth (Δ); Resulting distance distributions obtained with Tikhonov regularization with uncertainties (shaded grey areas) derived by varying the starting point of the background fit and the noise level. The traces are shaded to highlight the distance range in which the accuracy is not adequate, due to the maximal length of the trace detected.

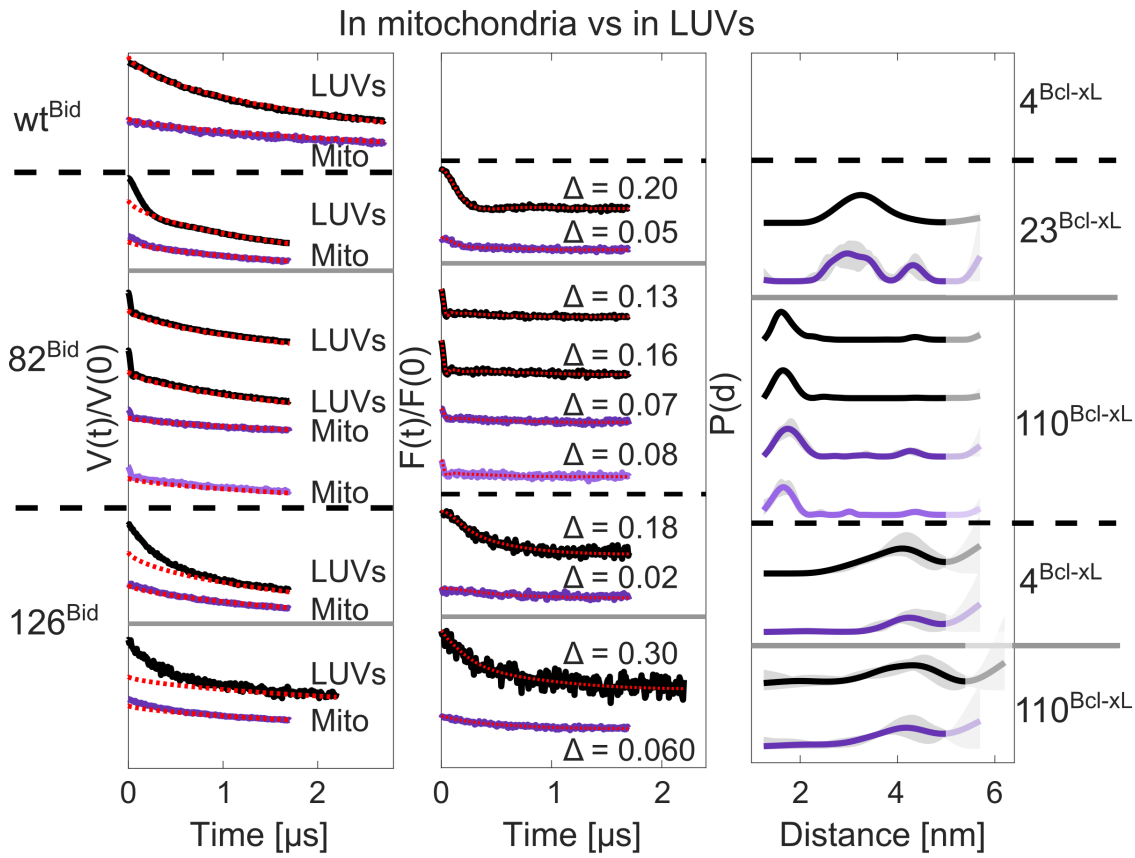

Figure S18: Comparison of *in vitro* and *in organelle* distance measurements. From left to right: Primary DEER data (black LUVs, purple mitochondria) with 2D-background fit (red dotted); Form factor obtained after dividing the primary data by the background (black/purple), fit (red dotted) and corresponding modulation depth (Δ); Resulting distance distributions obtained with Tikhonov regularization with uncertainties (shaded grey areas) derived by varying the starting point of the background fit and the noise level. The traces are shaded to highlight the distance range in which the accuracy is not adequate, due to the maximal length of the trace detected. Biological repeats are shown.

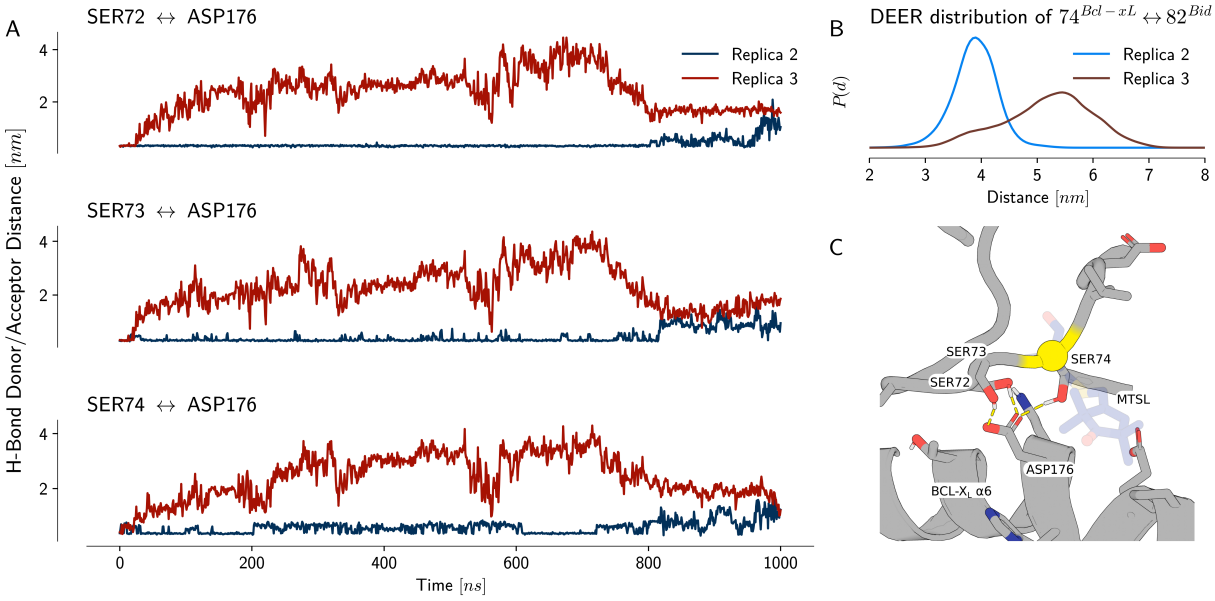

Figure S19: Interaction network of Bcl-xL-SER74. Forming transient hydrogen bonds with ASP 176 of Bcl-xL has a stabilising effect on the dynamics of Bcl-xL's $\alpha 1/2$ loop. Substitution with the MTSL label likely disrupts this interaction pattern and could result in a higher flexibility of the loop. **(A)** Time traces of Hydrogen Bonds between the Serines 72 to 74 and Aspartic acid 176 for two indipendent simulation replicates. **(B)** Predicted Deer distributions of the simulation replicates, here replicate 3 has better agreement with the experimental distribution. Replicate 3 constitutes most of the right tail of the total distribution shown in Fig. 5E. **(C)** Bcl-xL shown as grey cartoon with relevant side chains shown as sticks colored by atom type (oxygen red, carbon grey, nitrogen blue, hydrogen white) and hydrogen bonds indicated as dashed yellow lines. Representative MTSL placement shown as transparent blue sticks.

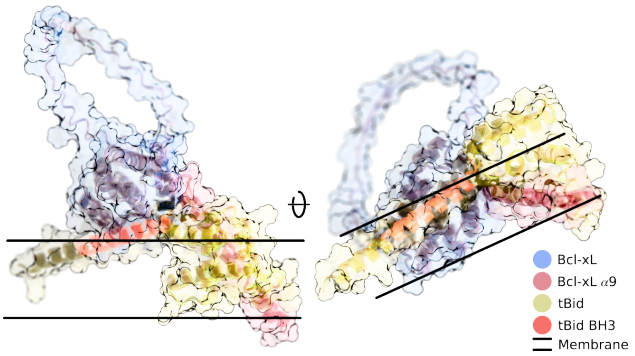

Figure S20: Alphafold model of the Bcl-xL/tBid complex. Protein complex shown as cartoon and surface colored by domain (globular Bcl-xL domain, TMD, tBid BH3 and tBid). Models were generated with ColabFold2.

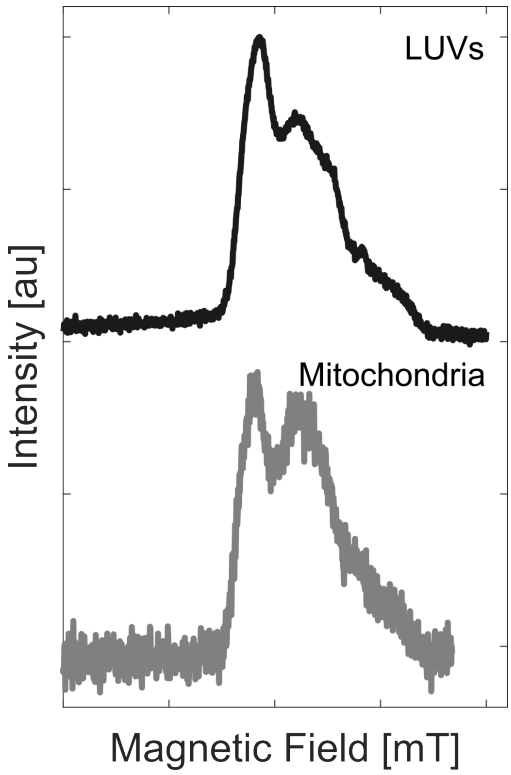

Figure S21: Field swept echo of LUV vs mitochondria samples showing the effects of metals on the field sweep. Sample: $110^{\text{Bcl-xL}}$ + 82^{Bid} pellet samples with either LUVs or mitochondria. Shot repetition time: 1 ms, t_1: 1000 ns, t_2: 400 ns, Sweep width: 20 mT, $\frac{\pi}{2}$-pulse: 18 ns, π-pulse: 36 ns.

Table S1: Tabulated contacts between tBid and Bcl-xL in MD simulations. Contact frequency was calculated as the ratio of MD frames ($\frac{1}{ns}$) where the contact was observed. Contacts are defined as a distance lower than 7 Å between the CoM of residue sidechains including hydrogen's. Relevant hydrogen bonds are indicated with red dots.

	tBid		Bcl-xL		
	Residue name	Residue position	Residue name	Residue position	Contact frequency
	Constant contacts $f_c > 0.8$				
	ILE	83	VAL	126	0.999
	ILE	86	LEU	112	0.913
	ALA	87	VAL	126	1.0
	ALA	87	GLU	129	0.941
	ALA	87	LEU	130	0.999
	HSD	89	TYR	101	0.898
	HSD	89	PHE	105	0.999
	LEU	90	PHE	97	0.995
	LEU	90	TYR	101	1.0
	LEU	90	LEU	108	0.973
	LEU	90	LEU	130	1.0
	LEU	90	ALA	142	1.0
	LEU	90	PHE	146	0.997
	ALA	91	LEU	130	1.0
	VAL	93	PHE	97	1.0
	VAL	93	TYR	101	1.0
	VAL	93	ALA	104	0.998
	VAL	93	PHE	105	0.852
	ASP	95	ASP	133	0.852
•	ASP	95	ASN	136	0.978
•	ASP	95	ARG	139	1.0
	MET	97	ALA	93	0.804
	MET	97	PHE	97	0.999
	MET	97	GLY	138	0.997
	MET	97	VAL	141	0.986
	MET	97	TYR	195	0.921
•	ASP	98	ASN	136	0.999
	ILE	101	LEU	194	0.898
	ILE	101	TYR	195	0.942
	Transient contacts $0.5 < f_c < 0.8$				
	ILE	82	HSD	113	0.58
	ILE	83	SER	122	0.732
	ILE	83	GLN	125	0.573
•	ARG	84	GLU	129	0.776
	ILE	86	VAL	126	0.666
	ILE	86	PHE	146	0.51
	ARG	88	GLU	129	0.605
	ARG	88	ARG	132	0.512
•	ARG	88	ASP	133	0.713
	ARG	88	ARG	139	0.616
	LEU	90	VAL	126	0.548
	MET	97	GLU	96	0.714
	MET	97	ARG	100	0.591
•	SER	100	ARG	100	0.797

	NO-NO
Shot repetition time [ms]	5
t_1 [ns]	400
t_2 [ns]	2000 - 6000
Zero time [ns]	120
t_1 averages in steps of [ns]	8 or 16

Table S2: Applied DEER parameters.

Video band width [MHz]	20
Shot repetition time [ms]	5
τ [ns]	304
T start [ns]	20
T increment [ns]	10
T increment steps	1000

Table S3: Applied ESEEM parameters.

Table S4: Simulation protocol and restraint used throughout. For detailed description on other simulation parameters see Methods.

System	integrator	nsteps	emtol	constraints	constraint algorithm	replicates
Holo	steep	50000	1000.0	–	–	1
Apo	steep	5000	1000.0	h-bonds	LINCS	4

Holo				Restraints $[kJ/mol]$							
	Step	Ensemble	Duration $[ns]$	Sidechain	Backbone	Lipid Z	Lipid dihed	Helix	CV	Continue	Repl
Equil.	0	NVT	0.125 (1fs)	1000	2000	400	400	–	–	No	1
	1	NPT	0.125 (1fs)	500	1000	400	200	–	–	No	1
	2	NPT	0.5 (2fs)	200	500	200	200	–	–	No	1
	3	NPT	1.0 (2fs)	0	100	40	0	–	–	No	1
ABMD	0	NPT	COMITTOR (2fs)	0	500[a]	0	0	5000.0	200.0[b]	No	1
	1	NPT	15.0 (2fs)	0	20	200[c]	0	0.0	0.0	No	1
Prod.	0	NPT	60.0 (2fs)	0	0	0	0	–	–	No	7
	1	NPT	1000.0 (2fs)	0	0	0	0	–	–	Yes	7

Apo				Restraints $[kJ/mol]$							
	Step	Ensemble	Duration $[ns]$	Sidechain	Backbone	Lipid Z	Lipid dihed	Helix	CV	Continue	Repl
Equil.	0	NVT	0.125 (1fs)	200	400	100	100	–	–	No	4
	1	NVT	0.125 (1fs)	1000	2000	400	400	–	–	No	4
	2	NPT	0.125 (1fs)	500	1000	400	200	–	–	No	4
	3	NPT	0.5 (2fs)	200	500	200	200	–	–	No	4
	4	NPT	1.0 (2fs)	0	100	40	0	–	–	No	4
	5	NPT	50.0 (2fs)	0	0	0	0	–	–	No	4
Prod.	0	NPT	200.0 (2fs)	0	0	0	0	–	–	No	4

[a] Bcl-xL only
[b] ABMD κ
[c] z-pos to z-CoM of each leaflet